New synthesis and surface treatments for high efficient nanophosphors

Ayse Dulda

The Graduate School

Sungkyunkwan University

Department of Nano Science and Technology

New synthesis and surface treatments for high efficient nanophosphors

Ayse Dulda

Thesis submitted to the Department of Nano Science and Technology and the Graduate School of Sungkyunkwan University in partial fulfillment of the requirements for the degree of Doctor of Philosophy

December 2009

Approved by

D.H. Yoon

Prof. Yoon Dae-Ho

[Major Advisor]

This certifies that the Ph. D. dissertation of A. Dulda is approved.

D.H. Yoon

Thesis Supervisor: Prof. Dae-Ho Yoon

Thesis Committee Head: Prof. Dae-Joon Kang

Thesis Committee Member: Prof. Dong-Mok Whang

Thesis Committee Member: Dr. Yoon Chang Kim

Thesis Committee Member: Dr. Sung Jei Hong

The Graduate School

Sungkyunkwan University

December 2009

To My Parents

Acknowledgements

There are many who have contributed to my success in the work presented here, and first among them are my Ph.D. advisors, Prof. Dae-Ho Yoon and Dr. Masaki Takaki, who challenged me throughout progress. I sincerely appreciate their trust and confidence. I am also indebted to my thesis committee head and members, Prof. Dae-Joon Kang, Prof. Dong-Mok Whang, Dr. Yoon Chang Kim and Dr. Sung Jei Hong for their invaluable discussions and insights, and critical reading of my work. I am very grateful to Prof. Kenji Toda for his collaboration, and fruitful discussions. I would also like to thank my colleague Deok-So Jo for his experimental help.

I would like to take this opportunity to thank Korean government for BK–21 and Samsung Advanced Institute of Technology for their financial support to the work presented here.

Finally, I would like to thank my parents and family members for their continuous support and encouragement. I specially thank my mother, Yeter, for her endless patience and support.

A. Dulda, December 2009

Preface

As optical interfaces between technology and humans, display devices play an indispensable role. In particular, plasma display panels (PDPs) have become prevalent enabling manufacture of large-sized displays for use in indoor and outdoor applications. Phosphors are very important factors influencing on PDP device performance. The particle size and morphology of phosphor particles play an important role for high resolution and good image quality. Nowadays, the size of commercial phosphors is in the micrometer range and there is a significant expectation of superior performance using nanosized phosphors to replace the existing commercial ones. In this dissertation, mainly new synthesis methods and surface treatment are studied for high efficiency in nanophosphors.

In Chapter 1, fundamentals and current applications of phosphors are briefly introduced. Chapter 2 gives a general overview of theory and background for luminescence and luminescent materials. The concept of configurational coordinate diagram model of luminescence centers is explained to better understand the spectral shapes of luminescence spectrum. On the basis of this model, the origin of spectral lines and broad bands are described. After absorption and emission process, energy transfer mechanism from localized and unlocalized centers is described and rare earth ions which are localized type luminescence center at the end of this chapter.

Chapter 3 and 4 constitute the backbone of this Ph. D study introducing new synthesis methods and surface treatments. In Chapter 3, a cellulose templated synthesis that we called liquid phase precursor (LPP) method is described and experimental flowcharts and schematic diagrams are provided to explain this process.

Unlike nanoparticles produced from "bottom-up" approach, their milling process can be conducted by a "top down" approach. Such nanoparticles exhibit a weak luminescence intensity as the milling process leads the formation of defects on the surface. Improvements in surface state of nanoparticles may also offer the practical and alternative approaches for high efficiency by eliminating the surface defects caused mostly by adsorbed chemical species or low crystallinity. Therefore, experiments that we perform for enhancement luminescence intensity related to surface treatments and functionalization of nanoparticles are presented in chapter 4. Finally, all those results were summarized in Chapter 5.

Contents

List of tables

List of figures

CHAPTER 1

Introduction

In modern society, people rely heavily on rare-earth based devices. In almost any office, light is produced by fluorescent lamps in which UV radiation from plasma is converted into visible light by rare-earth based phosphors. In addition, in our information society, vast amounts of information are read from displays. In this sense, plasma display panel has the potential to revolutionize the display technology by providing large and flat displays that can be hung on the wall. Since luminescent materials are a key component for this emissive display concept and lighting applications, research in the field of rear earth phosphors has been extensively studied to obtain ideal physical properties such as high brightness, good color quality, high UV absorption and quantum efficiency. Although activities to produce novel phosphors have almost come to an end, there is still room to further boost the PDP screen efficiency. It seems future work will concentrate on the improvement of a few standard materials in terms of particle size and morphology, surface design and high quantum efficiency.

For the application in plasma display panels (PDPs), phosphors with a high quantum efficiency and light output (high absorption, i.e. low reflection) under vacuum ultraviolet (VUV) excitation are required, since in these devices a Xe or Xe/Ne discharge emitting in the range 140–190 nm is employed. Well-known VUV phosphors that are nowadays used are $BaMgAl_{10}O_{17}$: Eu (BAM) as a blue-emitting phosphor, $LaPO_4$: CeTb, $CeMgAl_{11}O_{19}$: Tb (CAT), $GdMgB_5O_{10}$: CeTb (CBT) or Zn_2SiO_4 : Mn (ZSM) as a green-emitting one, and Y_2O_3 : Eu (YOE), $(Y,Gd)BO_3$: Eu (YGB), and $Y(V,P)O_4$: Eu (YVE) as a red-emitting one [1].

Herein, blue emitting BAM:Eu and red emitting $Y(V,P)O_4$:Eu phosphors are selected as standard materials and new synthesis and surface treatment concepts are introduced for high efficieny of phosphor particles at nanoscale.

There are numerous chemical methods for preparing nanomaterials; those including co-precipitation, sol-gel processing of colloids, spray pyrolysis, hydrothermal methods, gel processing of organic polymers or polymerizable media in the presence of metal complexes [2]. In this dissertation the author focuses on template based synthesis approach. The use of organic compounds as templates is realized and cellulose fiber or polymerized gel is employed since they have the unique characteristics of possessing many reactive functional groups. The presence of such functional groups makes cellulose or other polymeric gel a promising material to be used in stabilization of nanoparticles. In addition, immobilization of metal ions in such rigid organic polymer may reduce segregations of particular metal ions, thus ensuring the compositional homogeneity [3].

In the initial of synthesis part, liquid phase precursor method in which solid polymer network (cellulose pulp) is used as a template is presented. Secondly, gel routes involving formation of polymeric resin through the polyesterification process between metal complexes using an α-hydroxycarboxylic acid such as citric acid and propylene glycol is introduced. For the high efficiency not only intrinsic property of phosphor itself surface property also plays an effective role. Finally, we have performed surface treatment experiments and results are reported in Chapter 4.

CHAPTER 2

Theory and Background

A phosphor is a luminescent material that emits radiation when undergoes to energized particles such as electrons or ultraviolet photons. Excitation could be achieved by exposure to electromagnetic radiation (visible, ultraviolet, X-ray or gamma photon), particle beams (electrons, neutrons or ions) or as the case of semiconductors electrical current. Those are reflected in expressions the type of luminescence such as photo-, electro-, chemi-, thermo-, sono- or triboluminescence. In addition to excitation source, sometimes decay time (τ) is also used to classify luminescence; fluorescence (τ <10 ms) and phosphorescence (τ >0.1 s) [4]. Nowadays, luminescent materials are manufactured for variety of applications. This includes displays such as television tubes, computer monitor tubes, ossiloscopes, radar screens and displays in electron microscopes. There are also many lighting applications, such as standard fluorescent lamps and compact fluorescent lamps. The other important applications are X-ray intensifying and scintillation (e.g., for medical X-ray detection monitors) [5].

Most of phosphors are composed of a transparent host lattice and intentionally added impurity atoms (Figure 2.1.1). In general, the excitation energy is absorbed by the host lattice and subsequently transferred to activator ion or directly absorbed by activator ion. Then visible light is produced depending on the energy level position of activator ion and its interactions with host lattice. After absorption of excitation energy, the energy transfer process may occur in the fallowing way: migration of electric charge (electrons, holes), or migration of excitons, resonance between atoms with sufficient overlap integrals, reabsorption of photons emitted by another activator ion or sensitizer [4, 5].

2.1. Absorption process

As we mentioned above, a phosphor material consist of host lattice and activator ion, both of which play a role in defining electronic structure. When we consider host lattice (bulk crystal), a huge number of atoms located close enough to interact. In the absence of such interactions, the energy levels of each atom are well defined and separated. However, as the number of interacting atoms increases energy levels split, consequently, a single level in isolated atom is converted into a band structure that is continuum of closely spaced energy levels. Many different types of interactions are involved in holding atoms together. Those can be in ionic, covalent or relatively weak van der Waals character [6].

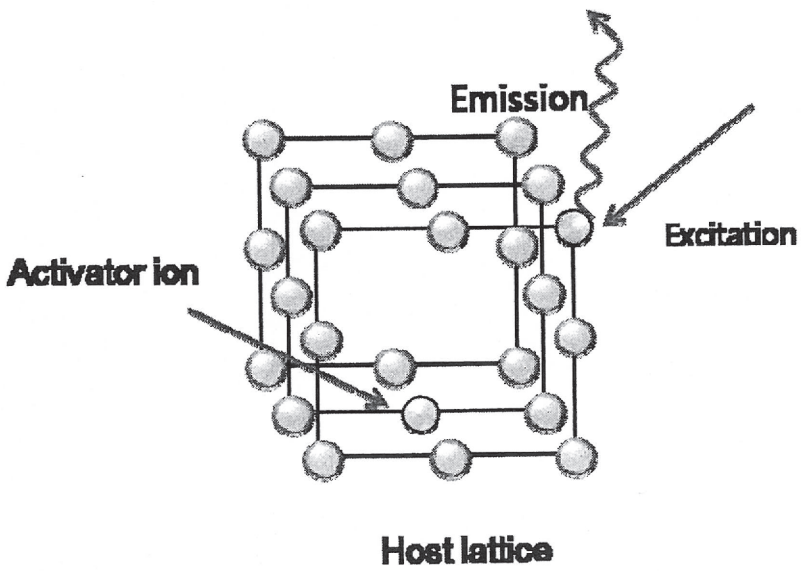

Figure 2.1.1 Light emission process in phosphor crystal

The shape of optical absorption band, narrow or broad, can be explained by using the configurational coordinate diagram (Figure 2.1.2). This diagram is built up from potential energy curves (vibrational energy modes) of absorbing center regarding its configurational coordinate. When we consider metal-ligand system as absorbing center, since the vibrations change instantaneous distance between metal and ligand ions, they influence energy of their electrons. For the simplicity, if we consider harmonic oscillator approximation in which the force F, and energy E, operating between the metal and ligand ions are related to $R-R_0$ displacement as fallow:

$$F=k(R-R_0) \quad (1)$$

$$E=1/2k(R-R_0)^2 \quad (2)$$

where k is the force constant.

The quantum mechanical solution of harmonic oscillator gives a series of vibrational energy levels for a specific electronic state in the fallowing form:

$$Ev=h\upsilon(\upsilon+1/2) \quad (3)$$

Energy is quantized into discrete states characterized by quantum number $\upsilon=0, 1, 2,\ldots n$. In figure 2.1.2 from first to nth vibrational levels of configuration are given along with the squares of wave functions which represent the probabilities of finding the system at the distance of R. These show that most probable position for the system is at R_0 distance between atoms, when $\upsilon=0$. As the υ value increases the edge of the parabola represents probable distance between atoms. This consideration is held for ground states of system. In

the case of excited state, since nuclear position of system may differ due to new electronic configuration, both equilibrium distance between atoms and the force constant k differ. However, as the case of lanthanides, 4f electrons are well shielded by outermost filled 6s and 5p orbitals and equilibrium distance between atoms will remain unchanged [7].

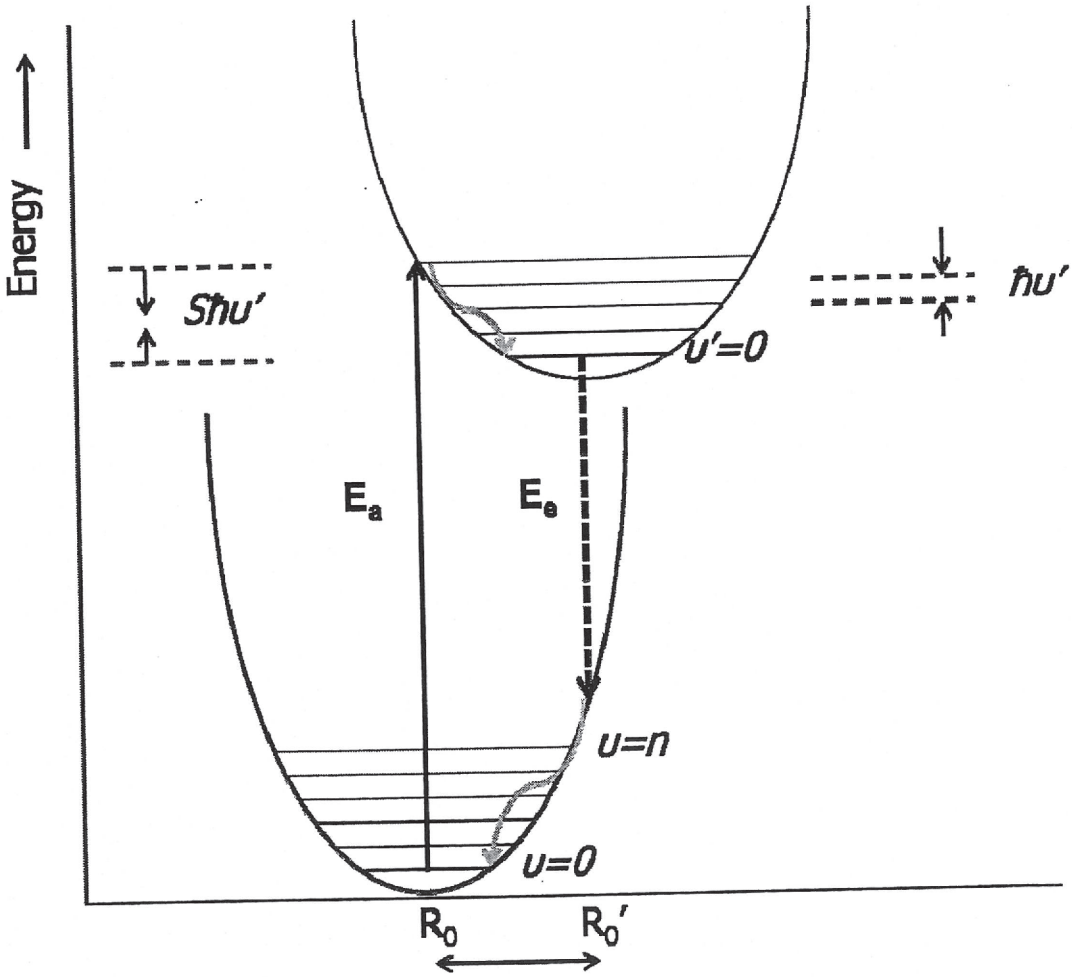

Figure 2.1.2 Configurational coordinate diagram

Figure 2.1.3 depicts the absorption process for both cases as discussed; the first (a) in which the parabolas for ground and excitation states are not shifted, (b) the parabolas exhibits a shift in equilibrium distance. As it was illustrated in both diagrams, the shape of absorption band strongly depends on the displacement between ground state and excited state of parabolas. The greater $R_0 - R_0$` displacement results in the broader absorption band [8].

To illustrate the effect of activator ion on the spectral shape of absorption spectrum Lu_2O_3 crystal was selected as host lattice and emissions from Eu and Tb dopand ions were examined (Figure 2.1.4) [9]. The narrow lines in both spectra arise from 4f configuration (intraconfigurational transitions) of Tb and Eu ions. However, origin of the broad band in the UV region differs for both spectra. In the case of Tb doped crystal, a broad band lying between 240-420 nm exhibits three peaks at 265, 290 and 305 nm due to interconfigurational $4f^8 \rightarrow 4f^7 5d$ transitions (Figure 2.1.4 (a)). After excitation, an electron has to be raised an orbital, beyond 4f configuration. An electron from the ground state of 4f configurations is being raised to one of the 5d states. This leads an expansion in the equilibrium distance between Tb-O ions. The situation is slightly different for Eu doped crystal. In this case broad band in UV region does not exhibit several peaks suggesting that it results from the charge transfer (CT) transitions. This kind of transition happens in metal-ligand system when an electron is transferred from orbital located on a ligand into orbital belonging to Eu3+. Here, the most important thing is that we have to point out how to distinguish CT state and $4f^{n-1}5d$ state. Although, both cases involve changes in the equilibrium distance between metal and ligand ion, the $R_0 - R_0{}^E$ displacement (Figure 2.1.4 (b)) is much larger in the CT case. This reflects on the absorption spectrum as a much broader line shape.

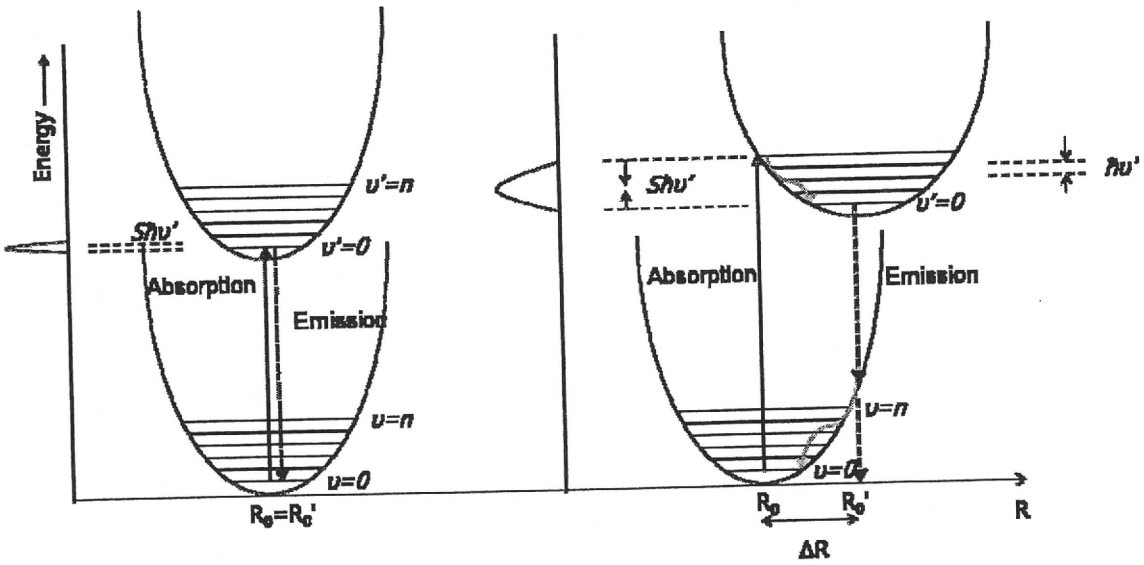

Figure 2.1.3 Schematic description of absorption process between the states in (a) same equilibrium distance (b)longer metal-ligand distance in excited state. This reflects as a band broadening on the spetrum.

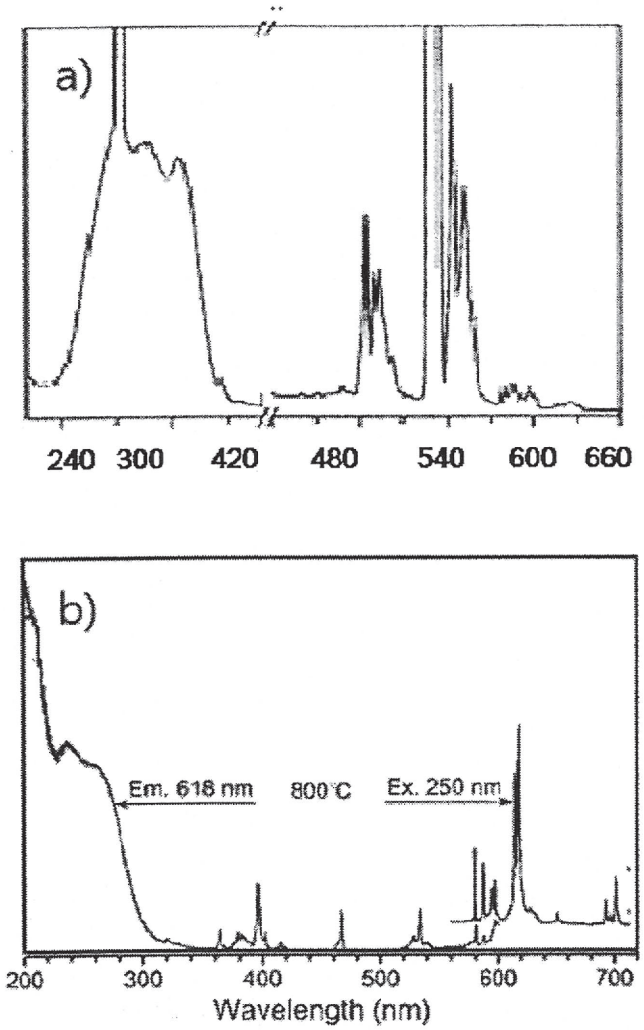

Figure 2.1.4 Excitation spectra of (a) Tb emission, (b)and red Eu emission[9].

When we consider host lattice absorption the situation is rather different. For example, as a result of optical absorption in ZnS free charge carriers (electrons and holes) are created in conduction and valance band. However, not every host lattice yields free carriers upon optical absorption. In the case of $CaWO_4$, under ultraviolet excitation energy is absorbed in the WO_4^{2-} groups and electrons (on oxygen) and holes (on the tungsten) remain bounded without dissociation. Their interaction energy is strong enough to prevent delocalization like in ZnS. Such a strongly bounded electron-hole pair is known Frenkel exciton. In the case of high energy excitation process such as cathode rays, X-rays or gamma rays, situation is rather complicated. After excitation, ionization occurs and many secondary electrons are released. When these electrons thermalised electron hole pairs remain as like in ZnS [9].

2.2 Emission process from a luminescent center

A common property of matter is that a system possessing excess energy seeks a way to release out of it. In the case of luminescent materials this may occur in two main group: (1) radiative and (2) nonradiative relaxation. In reality, light emission may occur in the presence of both relaxation and they influence material luminance quality.

It is obvious to make a simple subdivision into two classes of optical transitions which resulted in free charge carrier (electron and hole) and localized luminescence centers.

Luminescence can be categorized as unlocalized and localized types, regarding to whether excited electrons and holes (free charge carrier) of host lattice participate in luminescence process or whether excitation and emission process are confined to localized centers [8].

2.3 Unlocalized type luminescence

In semiconductors, most important impurities are donors and acceptors that dominate semiconductive properties, and those act as luminescence centers. There are two types of luminescence transitions, i.e., the transition of a bound electron at donor to bound hole at acceptor (donor –acceptor pair luminescence).

Donor –acceptor pair luminescence is an intermediate type between localized and unlocalized luminescence [8].

2.4 Localized type luminescence

When metallic impurities (activator) intentionally incorporated in a host crystal often create localized luminescence centers. Localized luminescence centers may exhibit (a) allowed type transition, and (b) forbidden type transition, in regard to electric dipole transitions.

The electric dipole transition can take place between energy levels with different parities. The selection rule for this transition in atoms is for the azimuthal quantum number $\Delta l = \pm 1$. When foreign atoms and ions incorporated in crystal, the forbidden character of dipole transition is altered by the perturbation of crystal electrical field, so that the forbidden transition becomes allowed to some degree. Here are the typical examples for localized type luminescence center.

(a) Allowed transition type,

(i) $s \leftrightarrow p$ transition $\rightarrow$ F center (an electron trapped at an anion vacancy)

(ii) $s^2 \leftrightarrow sp$ transition $\rightarrow$ Tl^+, Sn^{2+}, Pb^{2+}, Sb^{3+}, Bi^{3+}

(iii) $f \leftrightarrow d$ transition $\rightarrow$ Eu^{2+}, Ce^{3+}

Oscillator strengths of this types of transitions are of the order of magnitude of 10^{-1}- 10^{-3}.

(b) Forbidden transition type

(i) d ↔ d transition → Ti^{3+}, Cr^{3+},Cr^{4+}, Mn^{3+}, Mn^{4+}, Fe^{2+}, Fe^{3+}

(ii) f ↔ f transition → Pr^{3+}, Nd^{3+}, Sm^{3+}, Eu^{3+}, Tb^{3+}, Tm^{3+}, Er^{3+} (and other trivalent rare earth ions)

These transitions are partially allowed and oscillator strengths are 10^{-4}- 10^{-8}.

2.5 Rare earth phosphors

Lanthanide ions as light emitters are characteristic because of their sharp emission lines. In the free ions, underlying electric dipole *f-f* transitions are parity forbidden. In crystalline environments this restrictions is partially allowed by mixing with orbitals having different parity. This results in comparably long excited states lifetimes. Magnetic dipole transitions are not parity forbidden, however they exhibits rather lower oscillator strengths. Exceptions to these general rules are possible with transitions of *d-f* character and then show quite short lifetimes. For application in display, phosphors having slow transitions are unfavourable. On the other hand sharp emission spectra which were concentrated in the visible region may provide the optimization of luminous efficacy. In the case of red emitting phosphor in display application, aforementioned conditions can be achieved through the Eu^{3+} lanthanide ions [9, 10].

Figure 2.5.1 shows the energy levels of main activator ions used in phosphor materials.

2.5.1 Ce^{3+} luminescence

Although Ce^{3+} has very low transition energy, energy gap between 5d states to nearest level $^2F_{7/2}$ is large enough for efficient light emission (Figure 2.5.1). The luminescence depends strongly on the structure of the host crystal through the crystal field splitting of the 5d states and two emission peaks can be observed due to transition from $^2F_{7/2}$ and $^2F_{5/2}$ energy

levels of Ce ions. The decay time is the shortest in the lanthanides (10^{-7} to 10^{-8}) since $d \rightarrow f$ transitions are both parity allowed and spin allowed [9, 10].

2.5.2 Eu^{3+} luminescence

Luminescence in Eu^{3+} ion originates due to ${}^5D_j \rightarrow {}^7F_j$ transitions. The emission in the vicinity is due to magnetic dipole transitions from ${}^5D_0 \rightarrow {}^7F_1$, which is insensitive to local environment. However, emissions around 610-630 nm due to electric dipole transitions are induced by the lack of inversion symmetry at the Eu^{3+} site. If the inversion symmetry exists at the Eu^{3+} site, magnetic dipole transitions became stronger than electric dipole transitions (Figure 2.5.1) [11].

2.5.3 Eu^{2+} luminescence

Eu^{2+} usually gives broad band emission due to *f-d* transitions and exhibit short decay time. The wavelength positions of emission bands highly dependent on host lattice due to crystal field splitting of 5d levels. As the crystal field strength increases the emission bands shift towards to longer wavelength side (Figure 2.5.1) [11].

2.5.4 Gd^{3+} luminescence

Gd^{3+} ion has a half filled 4*f* shell which gives a sharp line luminescence at ~315 nm and can be used as sensitizer since energy levels of the charge transfer states are the highest among the rare earth ions (Figure 2.5.1) [11].

2.5.5 Tb^{3+} luminescence

The luminescence of Tb^{3+} ions due to $^5D_4 \rightarrow {}^7F_j$ transitions generally results in many sharp lines. $^5D_3 \rightarrow {}^7F_j$ transitions also may contribute to emission and intensities decreases as Tb^{3+} ion concentrations increase (Figure 2.5.1) [11].

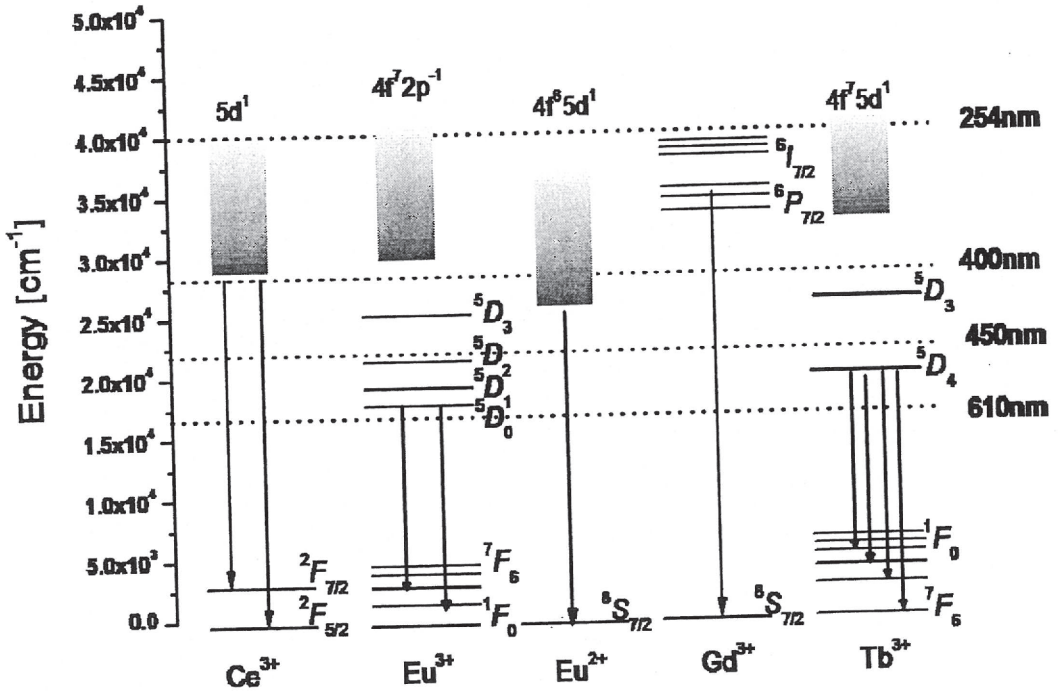

Fig. 2.5.1 Energy level diagram of rare earth ions

CHAPTER 3

Cellulose templated synthesis methods for phosphor nanoparticles

The basic idea behind the template based synthesis method is to use organic polymers, in the present study mostly cellulose, as a template due to their distinct nanosize porous structure. The abundant hydroxyl groups of cellulose not only anchor metal ions tightly in cellulose chain via ion–dipole interactions, but they also stabilize metal nanoparticles by strong bonding interaction with their surface atoms. Figure 3.1 illustrates the schematic description of stabilization of metal ions in a cellulose fiber. In this chapter, three different approaches are introduced for the preparation of phosphor nanoparticles according to template based synthesis method as follows.

i) Liquid phase precursor method,

ii) Polymerizable complex method,

iii) Hydrothermally polymerized gel method.

An important aspect of the aforementioned method is use of organic polymers having nanosize porous structure. This facilitates us to produce nanosize high efficient phosphor particles.

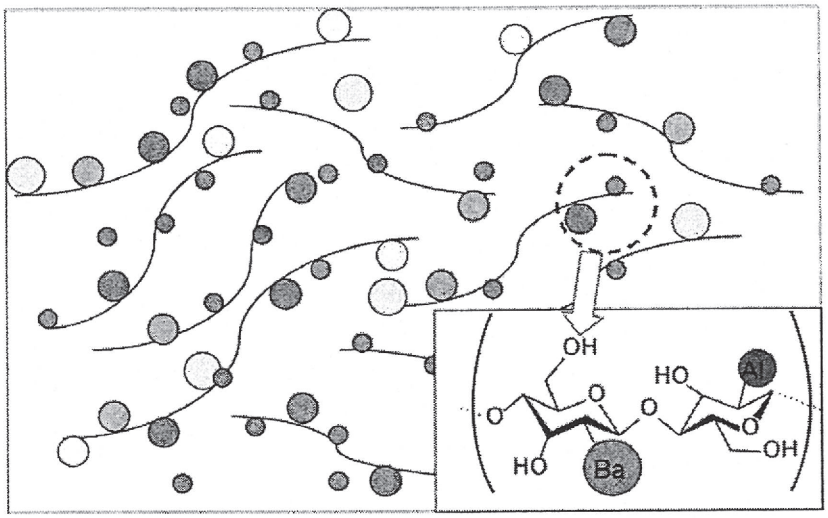

Figure 3.1. Schematic description of stabilization of metal ions in a cellulose fiber

3.1 Experimental

3.1.1 Liquid phase precursor (LPP) method)

In the LPP method a cellulose fiber was used as a template for the formation of phosphor nanoparticles. In this method, cellulose pulp was used to synthesize the nanoparticles due to the distinct porous structure of cellulose fibrils. It is expected that these pores may allow physical absorption of the metal ion contained in solution into the cellulose inner space. Most of the metal ions incorporated were bound to the cellulose chains probably via electrostatic (ion-dipole) interactions because the electron-rich oxygen atoms of the polar hydroxyl groups on the cellulose chains are expected to interact with the electropositive metal ions [12].

YPV:Eu phosphor synthesis: Raw materials; ($VO(SO_3)\cdot nH_2O$, $\geq$ 99.99 %), phosphoric (H_3PO_4, 99.99 %), yttrium chloride ($YCl_3\cdot 6H_2O$, $\geq$ 99.99 %) and europium chloride ($EuCl_3\cdot 6H_2O$, $\geq$ 99.99 %) were dissolved in deionized water. Aqueous solutions of those metal salts were mixed at a molar ratio of $Y_{0.99}P_{0.70}V_{0.50}O_4$:$Eu_{0.1}$, and 100 g of cellulose pulp was impregnated into 100 ml of the resulting mixture solution. The impregnated pulp was dried at 80 °C in a dry oven, and then rapidly calcined at 800 °C for two hours to remove the cellulose template. Finally, the calcined powder was heated from room temperature to 1150 °C at a heating rate of 200 °C. h^{-1} in air.

BAM:Eu phosphor synthesis: Raw materials, barium chloride ($BaCl_2\cdot 6H_2O$, $\geq$ 99 %), magnesium nitrate ($Mg(NO_3)_2\cdot 6H_2O$, $\geq$ 99 %), aluminum nitrate ($Al(NO_3)_3\cdot 6H_2O$, $\geq$ 99 %) and europium chloride ($EuCl_3\cdot 6H_2O$, $\geq$ 99.99 %) were dissolved in deionized water. The BAM solutions were prepared by mixing these metal salt solutions corresponding to the mol ratio of $Ba_{0.87\text{-}0.90}Mg_{0.95\text{-}0.91}Al_{10}O_{17\text{-}17.05}$:$Eu_{0.05}$. A cellulose pulp and BAM solution were used in the proportion of 1:1. The pulp was impregnated by inserting it into the mixed water solution and then dried at 80 °C in a dry oven to evaporate the water. The second step was conducted at 800 °C. The conditions were as follows: heating from room temperature to

800 °C a heating rate of 333 K / h^{-1}, maintaining the temperature at 800 °C for 1h and cooling to room temperature. At the last step, the calcined powder was heated from room temperature to 1400 °C at a heating rate of 333 K / h^{-1} under 5 % of H_2 containing N_2 atmosphere.

Aqueous solutions of those metal salts were mixed at a molar ratio of $Y_{0.99}P_{0.70}V_{0.50}O_4$:$Eu_{0.1}$, and 100 g of cellulose pulp was impregnated into 100 ml of the resulting mixture solution. The impregnated pulp was dried at 80 °C in a dry oven, and then rapidly calcined at 800 °C for two hours to remove the cellulose template. Finally, the calcined powder was heated from room temperature to 1150 °C at a heating rate of 200 °C. h^{-1} in air.

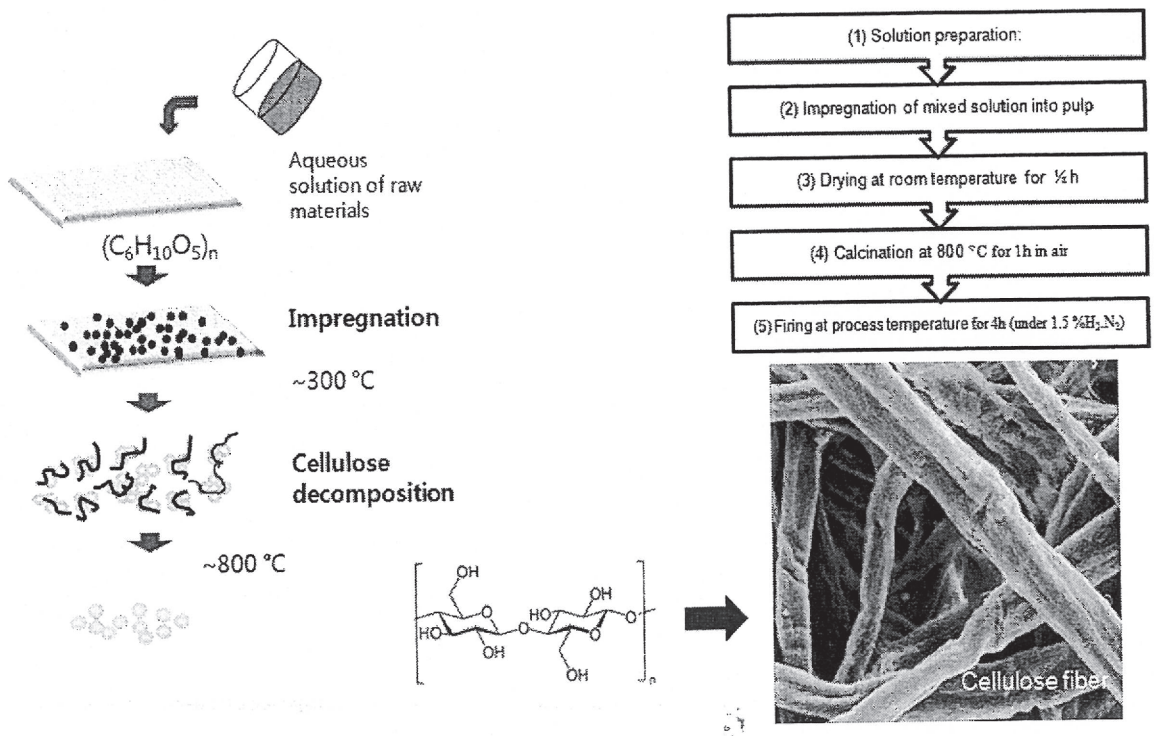

Figure 3.1.1.1. A schematic representation of the impregnation process

3.1.2 Polymerizable complex method

The basic chemistry involved in PC method is based on the formation of metal complexes with polymer network through the esterification reactions between α-hydroxycarboxylic acid and polyhydroxy alcohol. This method was first invented in 1967 by Pechini and closer approaches have been developed by Anderson et al. [13] and Zhang et al [14]. Recently, Kakihana's group also successfully synthesized high performance multicomponent oxide materials ranging in size from ~30 to ~250 nm modifying aforementioned methods. According to PC method, esterification reactions occur in the presence of citric acid and propylene glycol as shown in fallowing formula.

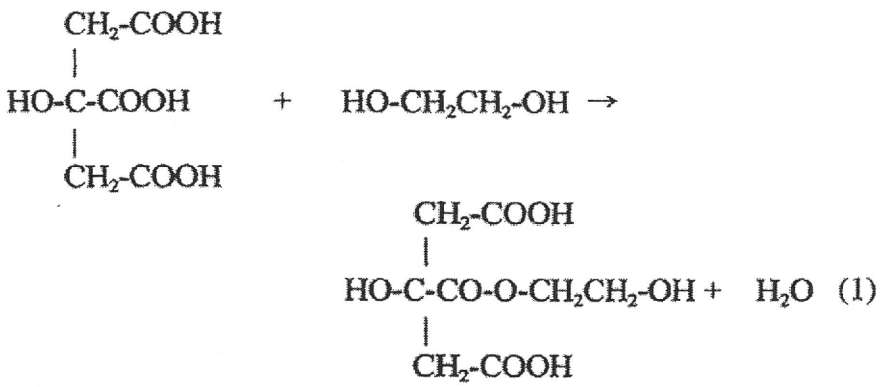

Upon heating, citric acid undergoes esterification reaction with glycol. Then chain formations begin. However resulting product still contains (OH) and (COOH), so that it can react further with glycol or citric acid to form polymeric resin (network type structure).

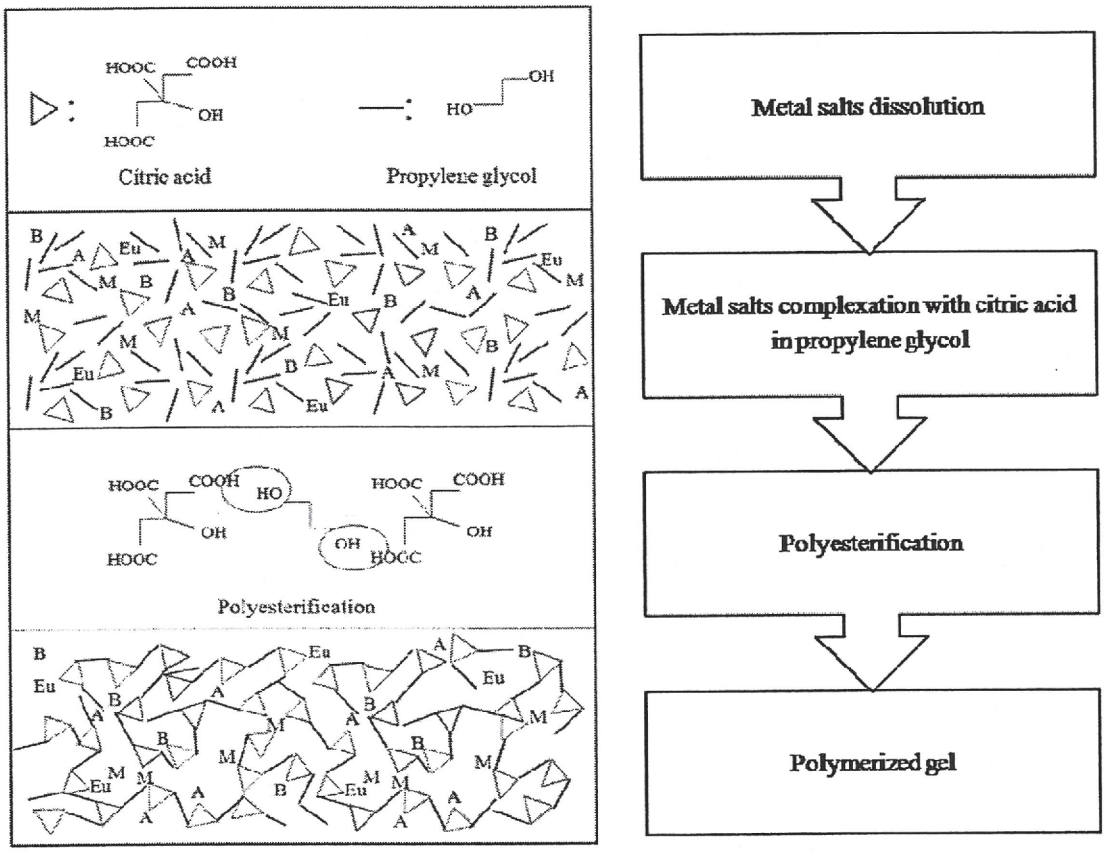

Figure 3.1.2.1. Ilustration of polymerizable complex method

BAM:Eu phosphor synthesis: The BAM solutions were prepared by mixing these metal salt solutions corresponding to the mol ratio of $Ba_{0.87}Mg_{0.91}Al_{10}O_{17}:Eu_{0.05}$ as outlined in Figure 3.2.2. $BaCl_2$, $Mg(NO_3)_2$ and $Al(NO_3)_3$ were selected as starting metal sources. Propylene glycol (PG) and methanol (MeOH) were used as solvents, and anhydrous citric acid (CA) was used as a chelating agent to stabilize Ba, Mg, and Al ions. $BaCl_2$, $Mg(NO_3)_2$ and $Al(NO_3)_3$ were first dissolved in MeOH, followed by the addition of CA and PG with continuous stirring at 80 °C. After achieving complete dissolution, heating temperature was increased to at ~130 °C to promote polymerization between CA and PG, while stirring continue. The solution became more viscous with time, and finally after several hours a honey-like gel was obtained without any visible precipitation. The honey like gel was heated at 300 °C for two hours and resulting powder was ground and heated at 800 °C to remove residual solvents and to burn out unnecessary organics. Note that 1 batch was prepared for 5 gr oxide. This can guarantee no deviation from the initially fixed metal composition in the starting solution.

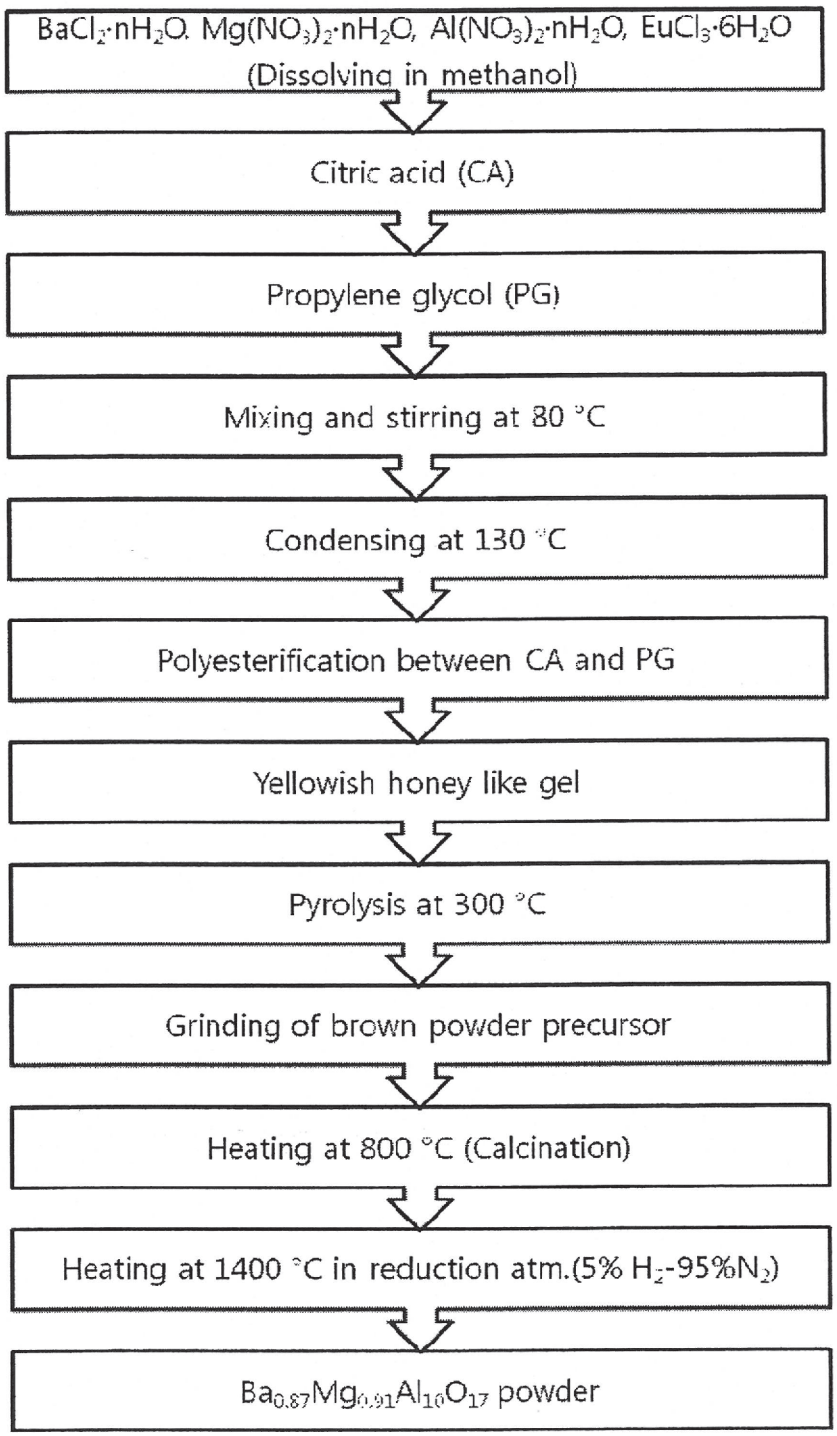

Figure 3.1.2.2. Flowchart for the polymerizable complex procedures

3.1.3 Hydrothermally polymerized gel method

Herein, Eu doped blue emitting BAM phosphor was synthesized by combining PC method with hydrothermal treatment. In this process, our aim is to preserve homogeneous metal ion distribution by using PC method and provide crystalline powder formation at lower temperature using autoclave.

BAM:Eu phosphor synthesis: Carboxymethyl cellulose (CMC) is selected for the formation of polymeric template as outlined in Figure 4.2.1. 0.5 gr CMC were dissolved in citric acid containing water mixture. Predetermined mol ratio of $BaCl_2$, $Mg(NO_3)_2$ and $Al(NO_3)_3$ of metal sources were dissolved in methanol to obtain $Ba_{0.87}Mg_{0.91}Al_{10}O_{17}:Eu_{0.05}$ compound followed by the addition of CMC-citric acid complex with continuous stirring at 80 °C. After achieving complete dispersion of partially misseble CMC, heating temperature was increased to at ~130 °C to promote polymeric gel formation. The solution became more viscous with time, and finally after several hours a honey-like gel was obtained without any visible precipitation. The honey like gel was sealed in a teflon lined autoclave and heated at 200 °C for 5 hours. The resulting powder was washed with ethanol several times to remove residual solvents and unnecessary organics. Finally, the present sample dried at 80 °C and heated at1400 °C for 4h in reduction atm. ($5\%H_2$-$95\%N_2$).

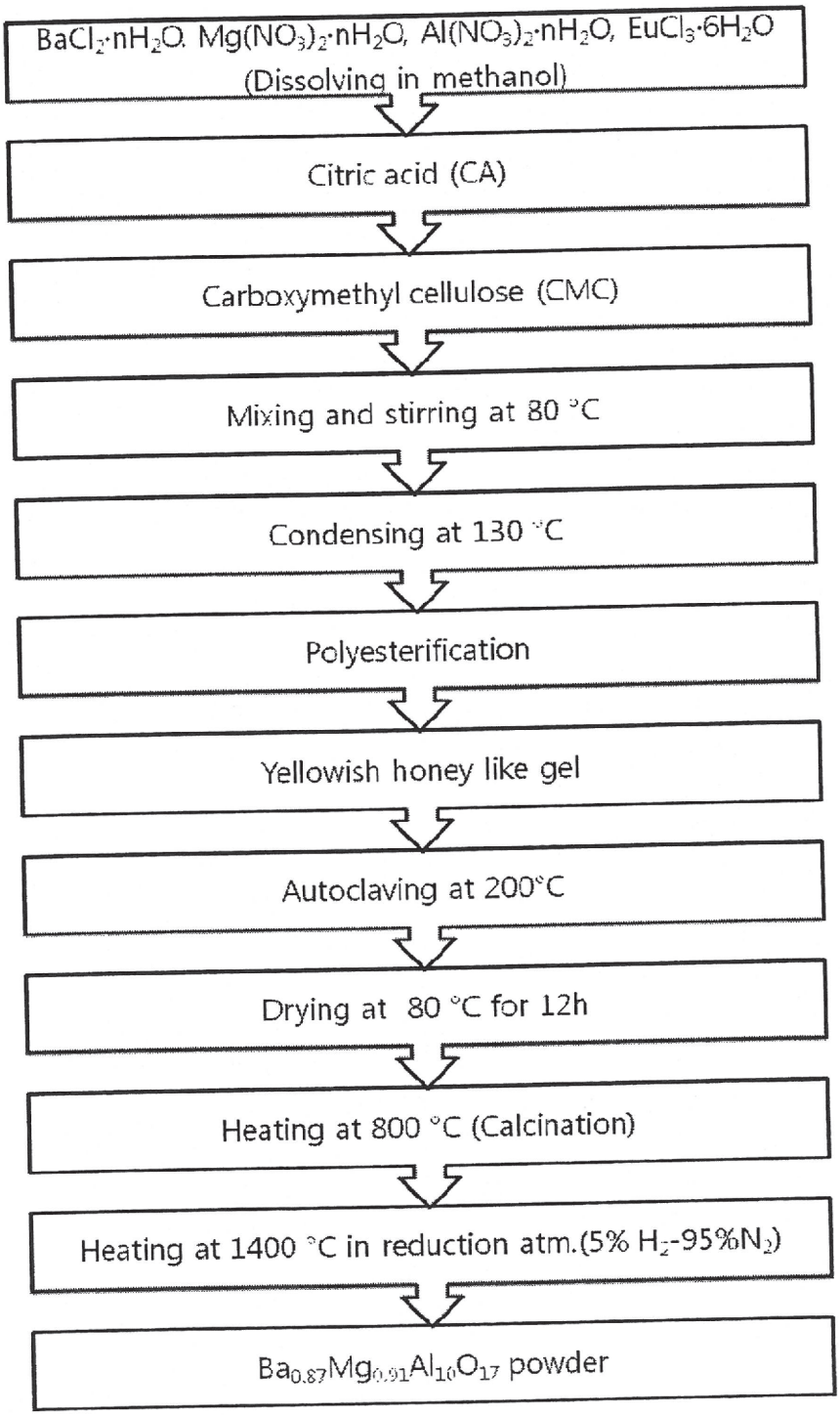

Figure 3.1.3.1. Flowchart for the PC combining hydrothermal treatment procedures

3.2 Results and discussions

3.2.1 YPV:Eu nanosized phosphors by LPP method and their luminescence properties

Field emission scanning electron microscopy (FESEM) was used to examine the morphology and particle size of the sample and commercial product. In the case of the present sample, the particles were spherical in shape and ~200 nm in size. In contrast, the commercial product showed large irregular shaped particles, ~5-7 μm in size (Figure 3.2.1.1 (a, b)).

Figure 3.2.1.2 shows HRTEM micrographs of $Y_{0.99}P_{0.70}V_{0.50}O_4:Eu_{0.1}$ sample revealing smooth surface and perfect crystalline structure with well defined lattice fringes (Figure 3.2.1.2(a, b)).

The XRD patterns of the $Y_{0.99}P_{0.70}V_{0.50}O_4:Eu_{0.1}$ sample (Figure 3.2.1.3) showed that a pure tetragonal xenotime phase was obtained and all recorded peaks were between the standard YVO_4 (JCPDS, 72–0274) and YPO_4 (JCPDS, 11–0254) pattern, agreeing with the Vegard law [15].

Figure 3.2.1.4 shows the excitation (λem= 618 nm) and emission spectra (λexc= 254 nm) of the $Y_{0.99}P_{0.7}V_{0.5}O_4:Eu^{3+}$ samples. In these figures, the luminescence intensities were normalized with respect to the micron sized commercial product. The excitation spectrum exhibited a broad band extending from 225-350 nm, corresponding to the charge transfer from oxygen ligands to the central vanadium atom insides the $VO4^{3-}$ group ions and weak bands at 380 and 395 nm in the longer wavelength region, originating from the f-f transitions of the Eu^{3+} ions (Figure 3.2.1.4(a)).The intensity of those peaks was weak because of multiphonon relaxations [16]. Figure 3.2.1.4(b) shows the emission spectrum (λ_{exc}= 254 nm) of the YPV:Eu powder synthesized using LPP method at 1150 °C. The emission spectra consisted three peaks assigned to $^5D_0$–$^7F_1$ (magnetic dipole transition) and $^5D_0$–$^7F_{2,4}$ (forced electric dipole transitions). The samples exhibited ~100.5 % emission intensity at 621 nm

compared to the micron-sized commercial product without line broadening. The strong luminescence intensity was attributed to a $^5D_0$–$^7F_2$ transition due to the absence of inversion symmetry at the Eu^{3+} lattice sites [17]. According to Judd-Ofelt theory, the intensity of transitions different J-number levels depends on the local environment of europium ion. It was reported that the ratios of the integrated intensities of $^5D_0$–$^7F_2$ and $^5D_0$–$^7F_1$ transitions under ultraviolet (UV) excitation can be considered indicative of the asymmetry of the coordination polyhedron of Eu^{3+} ion as $^5D_0$–$^7F_2$ transitions are hypersensitive [18-21]. Table 3.1.3 shows the calculated asymmetry ratios (R) of the micron sized commercial product, the present sample and previous work [22]. The size of present sample is comparable to that of previous one, but at least ten fold smaller than that of commercial product. It was expected that the differences in particle size may induce changes in crystal field experienced by Eu^{3+} ions as a large fraction of Eu^{3+} ions would reside on or toward the surface of nanoparticles [23]. However, the R value of the present sample is comparable to commercial product. In the case of previous work this value is ~2 fold larger indicating the higher asymmetry of Eu^{3+} ions due to structural distortions. On the other hand, even if structural distortion exists on the surface it should appear as line broadening on the luminescence spectrum [24]. Those results suggest that the present sample exhibits high crystallnity as a concequence of high synthesis temperature and, less structural distortions because extra thermal energy released during the burning of cellulose enhance the incorporation of Eu^{3+} ions into the inner shell of the particle surface.

Table 3.2.1.1. Calculated asymmetry ratios for the YPV:Eu sample and commercial produc

	Particle size	*$^5D_0$–$^7F_2$ / $^5D_0$–$^7F_1$ Asymmetry ratio*	*Efficiency*
$Y_{0.99}P_{0.70}V_{0.50}O_4$:$Eu_{0.1}$	~200 nm	3.98	100.5%
YPV(Commercial)	5-7 μm	2.78	100%
YPV(Ref 4)	30-250 nm	~6	~20%

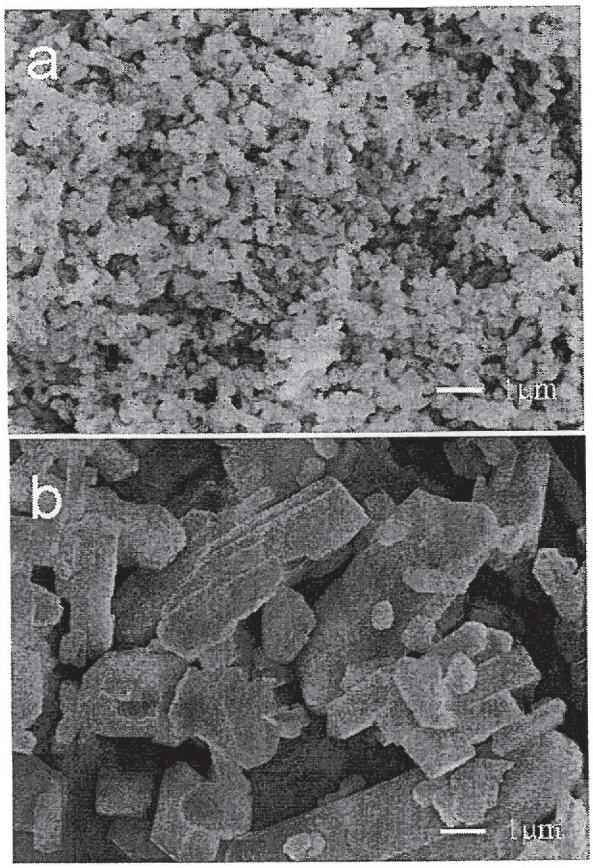

Figure 3.2.1.1. FE-SEM images of the $Y_{0.99}P_{0.7}V_{0.5}O_4:Eu^{3+}$ samples and commercial product

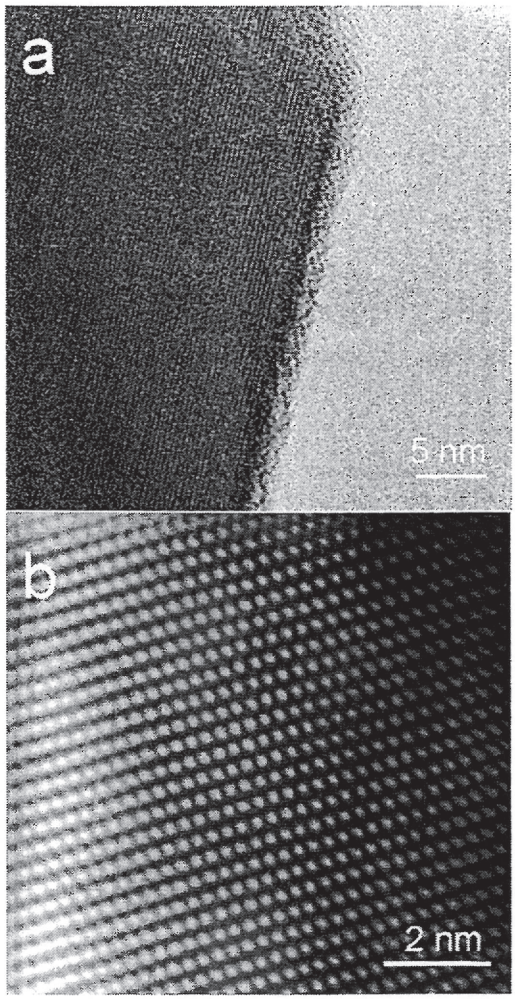

Figure 3.2.1.2. HR-TEM observations of the $Y_{0.99}P_{0.7}V_{0.5}O_4:Eu^{3+}$ samples (a) surface state and (b) lattice structure.

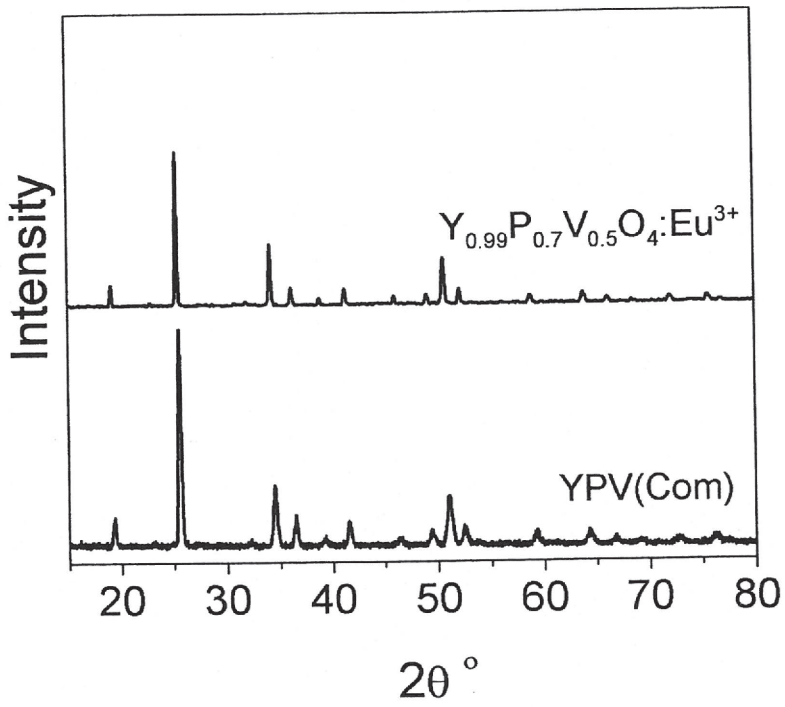

Figure 3.2.1.3. XRD patterns of the $Y_{0.99}P_{0.7}V_{0.5}O_4:Eu^{3+}$ sample synthesized by LPP method at 1150 ℃.

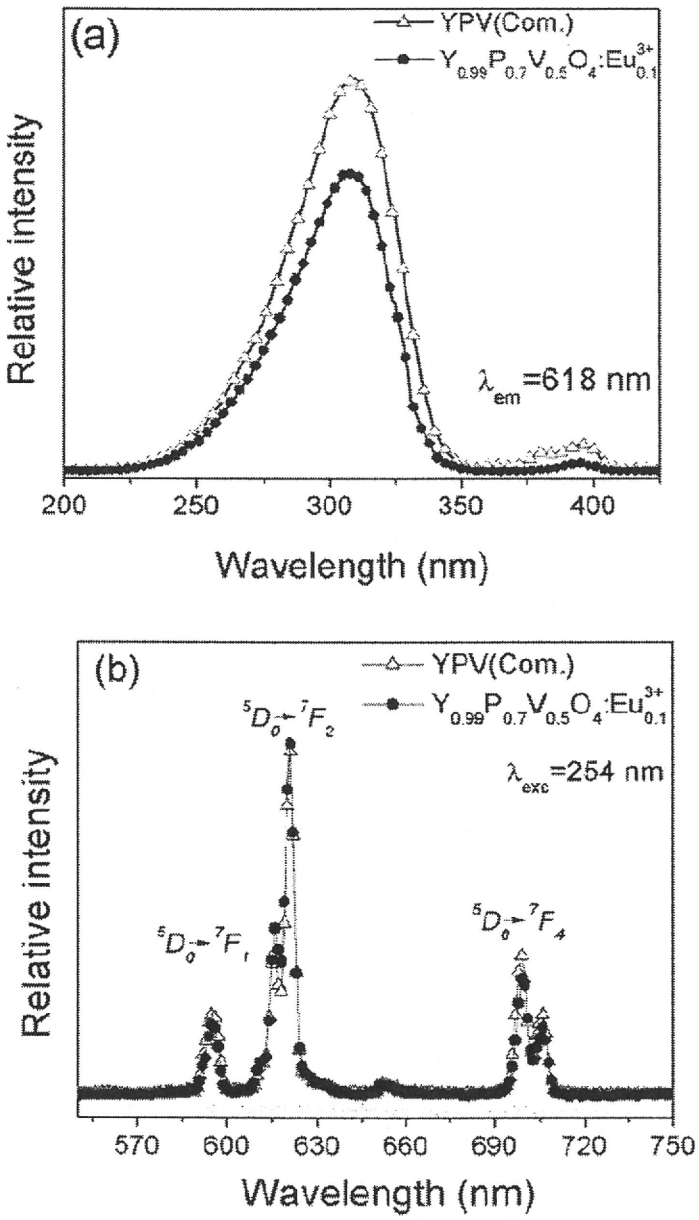

Figure 3.2.1.4. Room temperature (a) excitation and (b) emission spectra for $Y_{0.99}P_{0.7}V_{0.5}O_4:Eu^{3+}$ sample. Sample luminescence intensities were normalized with respect to commercial product.

3.2.2 BAM:Eu nanosized phosphors by LPP method and their luminescence properties

Blue emitting Eu^{2+} doped BAM phosphors have been widely used in fluorescent lights (FL) and plasma display panels (PDPs) [25-28]. Despite recent efforts to fabricate PDPs with a large screen, low energy consumption and wide viewing angle, some problems still exist to provide optimum brightness, color purity and resolution. Small-sized phosphor particles with good dispersibility have advantages for patterning small pixels. Small pixels with a high packing density contribute to obtain is high resolution and luminescence efficiency. All of these factors are influenced by the phosphor material itself or by the morphology of the phosphor layer. The porosity of the layer determines whether Vacuum Ultraviolet (VUV) photons can be transmitted through the phosphor layer. For instance, the existence of pinholes results in the absorption of VUV photons at the back plate leading to a reduction of the pixel efficiency. Therefore, the phosphor layer should be optically dense. This is optimally achieved with small (2~4 μm) and spherical particles [29].

Apart from the morphology, further improvement on the luminescence efficiency can be achieved by studying the defect mechanism. The earlier studies reported that a profound influence on the luminescence efficiency of Eu2+ doped BAM was obtained by a compositional variation or by introducing defects [6, 12]. The ternary phase diagram for the BaO–MgO–Al_2O_3 system was reported by Goebbels et al. [30] and solid solutions between BAM and $Ba_{0.75}Al_{11}O_{17.25}:Eu^{2+}$ (BAL) were prepared to provide some important insight into the relationships between the structure and the compositional change. BAL has been known as a highly Ba^{2+} deficient aluminate which forms at the end of the solid solution of Ba-poor hexagonal aluminates. The hexagonal aluminates are classified as the β-alumina and magnetoplumbite type structures. Both types consist of spinel blocks and conduction layers. The difference in the atomic arrangement of the conduction layer defines the type of structure. Generally, the emission peaks of hexagonal aluminates shifts in the longer wavelength as the

type of structure alters from magnetoplumbite to β-alumina. In addition, by changing the composition from BAM to BAL, emission peaks shift towards the same direction [31, 35].

So far, commercialized BAM has been prepared by a solid state reaction method with high luminescence intensity. However, this method has some disadvantages, such as inhomogeneous dispersibility of the dopant ions, the formation of polyhedral shaped large size particles [36]. Our aim in this paper is to develop BAM phosphors with high luminescence efficiency of nanosize, and also to control the particle morphology.

The emission spectrum was measured at room temperature using a Kr-excimer lamp as a source of Photoluminescence (PL) spectrophotometer in the ranges of 350–700 nm for 200 msec. under 2.664 X 10-3 Pa. The excitation spectrum was measured using a deuterium lamp and a VUV monochromator in the ranges of 120–340 nm with 2 nm scanning step. A powder X-Ray Diffractometer (XRD, Cu Kα, 30 kV, 100 mA, Rigaku) was used to determine the crystalline phases of synthesized specimens. The morphologies of the phosphor particles were observed using a Field-Emission Scanning Electron Microscope (FESEM, JEOL JSM6700F).

Figure 3.2.2.1shows the XRD pattern of the BAM specimens. The diffraction peaks are in agreement with the XRD pattern of barium magnesium aluminum oxide registered in JCPDS card No: 26-0163 with a hexagonal crystal structure in the space group $P6_3/mmc$. These peaks are less intense and broader due to their crystallite sizes compared with the commercial product.

Figure 3.2.2.2 shows a FESEM image of the rod shaped BAM particles contained within thin layers. The rod shaped phosphor particles were crystallized in a particular direction; in this case, horizontally along the thin layer. It can be assumed that this type of morphology is developed due to the micro fibrous structure of the pulp. The pulp was used as a template to alleviate the agglomeration of the particles and to restrict the crystal growth direction. By

inserting the pulp into the BAM solution, liquid nano-droplets that will be the seeds of the nano-sized particles are impregnated into the pulp, owing to the pulp's micro fibrous structure [37]. The impregnated liquid nano-droplets are surrounded by the fiber walls. Therefore, the nano-droplets tend to crystallize along the direction of the fiber until another fiber intersects it. During the initial step of the calcination process, the growth speed is fast and, therefore, the growth is suppressed by the pulp until it vaporizes at around 600 °C [38], then growth continues in the free space.

Figure 3.2.2.3 shows the FESEM images of the rod shaped phosphor particles having the compositions of (a) BAM-11, (b) BAM-12 and (c) BAM-13 as shown in table 1. They have a similar morphology, but their particle size slightly differs. The diameter of individual rod shaped nano-phosphor particles varies in the range of 60-100 nm and 400-700 nm in length.

Figure 3.2.2.4 shows the PL emission spectrum of BAM specimens and the commercial BAM phosphor excited at (a) 147 and (b) 254 nm. The commercial BAM phosphor has a broad emission band with a maximum of around 450 nm corresponding to the blue emission in visible region of the electromagnetic spectrum. This broad band originates due to the transitions of Eu^{2+} ions from the $4f^6 5d^1$ excitation state to the $4f^7$ ground state. However, our specimens have a peak shift towards the longer wavelength direction at around 465 nm in both emission spectra. Our specimens, labeled BAM-11 ($Ba_{0.90}Mg_{0.95}Al_{10}O_{17.05}:Eu_{0.05}$), BAM-12 ($Ba_{0.88}Mg_{0.93}Al_{10}O_{16.96}:Eu_{0.05}$), and BAM-13 ($Ba_{0.87}Mg_{0.91}Al_{10}O_{16.93}:Eu_{0.05}$) each have a non-stoichiometric composition. A shift in the emission band towards a longer wavelength direction was obtained as the concentration of Ba and Mg ions decreased. This type of shift can be called a red shift because the red wavelength is the end of the visible electromagnetic spectrum. In our specimens, the red shift increased due to Eu-O associations. As the concentration of Ba^{2+} or Mg^{2+} ions decreases in the composition, O^{2-} ions replace the Ba sites. This results in a variation in the crystal field of Eu^{2+} ions. The red shift was obtained

on the both emission spectra because the interactions of Eu-O complexes in such short distances suppress the position of the excited 5d levels to the lower energy position. On the other hand, when Eu ion has multiple location in crystal, a line broadening may occur in emission spectrum because multiple location of Eu ion effects the crystal field [35, 37]. Apart from the red shift, another notable feature is the decrease of the maximum emission intensities of our specimens on the PL spectra excited at 147 and 254 nm compared with the commercial BAM. It is suggested that the presence of Ba^{2+} vacancies made the emission intensity drop in our specimens as shown in fig. 3.2.2.4. Stevels [39] reported that the deficiency of Ba^{2+} ions in the conduction layer may cause a decrease in the emission intensity because the deficiency of Ba^{2+} ions may lead to formation of traps. The absorption of UV photons from these traps causes the decrease in the luminescence intensity. This explains why the luminescent intensity is very low when the Ba^{2+} is highly deficient in BAM phosphors. On the other hand, the substitution of O^{2-} ions for Ba^{2+} sites leads to the migration of Al^{3+} ions next to the conduction layer to compensate the charge neutrality. This may cause a formation of the Al-O-Al bridges, the so-called Reidinger defects. The formation of Reidinger defects leads to a decrease of intensity due to the non-radiative transitions [35]. The particle size also primarily affects the luminescence efficiency. As the particle size decreases the defects on the surface will increase due to the larger surface area of the smaller particles. In our experimental results, 80 % of PL intensity was obtained as shown in figure 3.2.2.4. It is expected that this lower intensity originates from the defects on the surface of the smaller particles.

Figure 3.2.2.5 shows the relative emission intensities of BAM specimens under 147 and 254 nm wavelength excitations. It was found that there was essentially no big difference in the emission spectra between that excited at 147 and 254 nm. It is expected that the energy transfer takes place via exciton emission because there is no big difference in the relative

intensities of the emission centers in both emission spectra, if the transfer mechanism was dependent on the local Eu^{2+} environments [34].

Figure 3.2.2.6 shows the excitation spectra of BAM specimens. It was found that the excitation mechanism of each specimen showed a different behavior as the excitation wavelength changed. As shown in fig. 3.2.2.6, there are three regions in the excitation spectrum. The first region extends from 125 to 147 nm where the excitation takes place through the spinel block. In the second region, the excitation takes place into the Ba^{2+} 5d level and energy transfer comes true over self-trapped exciton (STE) at Ba-O groups in between 147 to 185 nm; beyond 185 nm, excitation takes place directly at Eu^{2+} via $4f^7 \rightarrow 4f^6 5d$ transitions. Beyond 185 nm the samples have similar spectral shapes since all samples have the same Eu^{2+} ion concentrations [40].

Table 3.2.2.1. BAM compositions of specimen's in mol percent

Specimen compositions (mol %)	Code
0.90 BaO + 0.95MgO + 5 Al_2O_3 + 0.05 Eu_2O_3	BAM-11
0.88 BaO + 0.93MgO + 5 Al_2O_3 + 0.05 Eu_2O_3	BAM-12
0.87 BaO + 0.91MgO + 5 Al_2O_3 + 0.05 Eu_2O_3	BAM-13

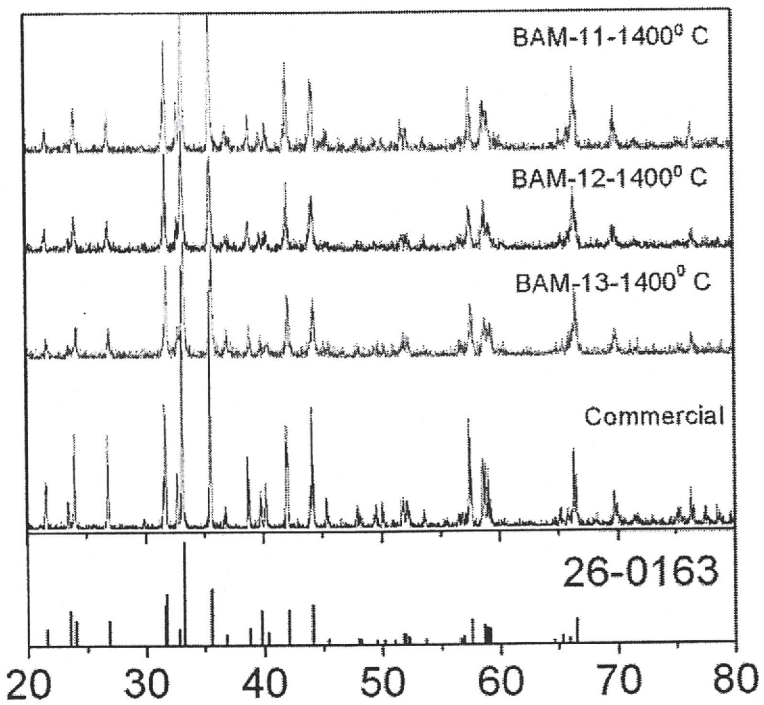

Figure 3.2.2.1. The XRD patterns of commercial $BaMgAl_{10}O_{17}:Eu^{+2}$ phosphor and BAM specimens prepared at 1400° C with different composition (BAM11, BAM12, BAM13) and spectral lines of $BaMgAl_{10}O_{17}$ registered in JCPDS card no: 260163 .

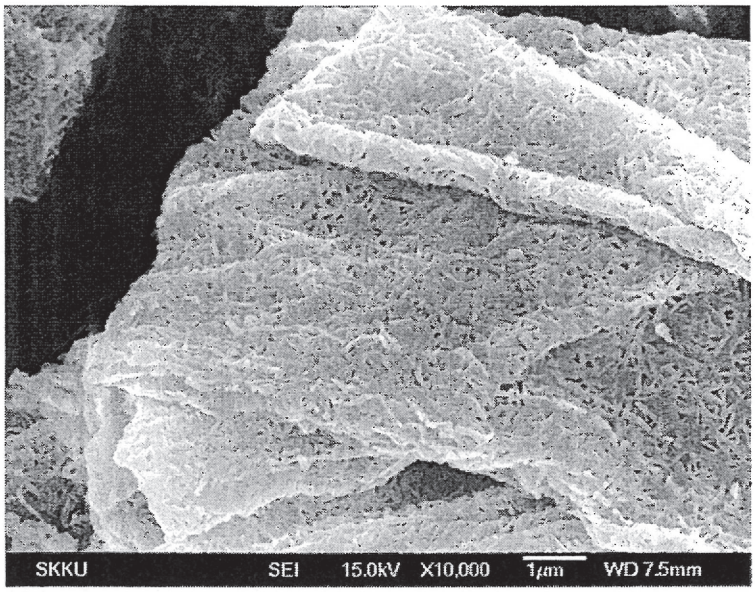

Figure 3.2.2.2. FESEM image of the rod shaped BAM particles.

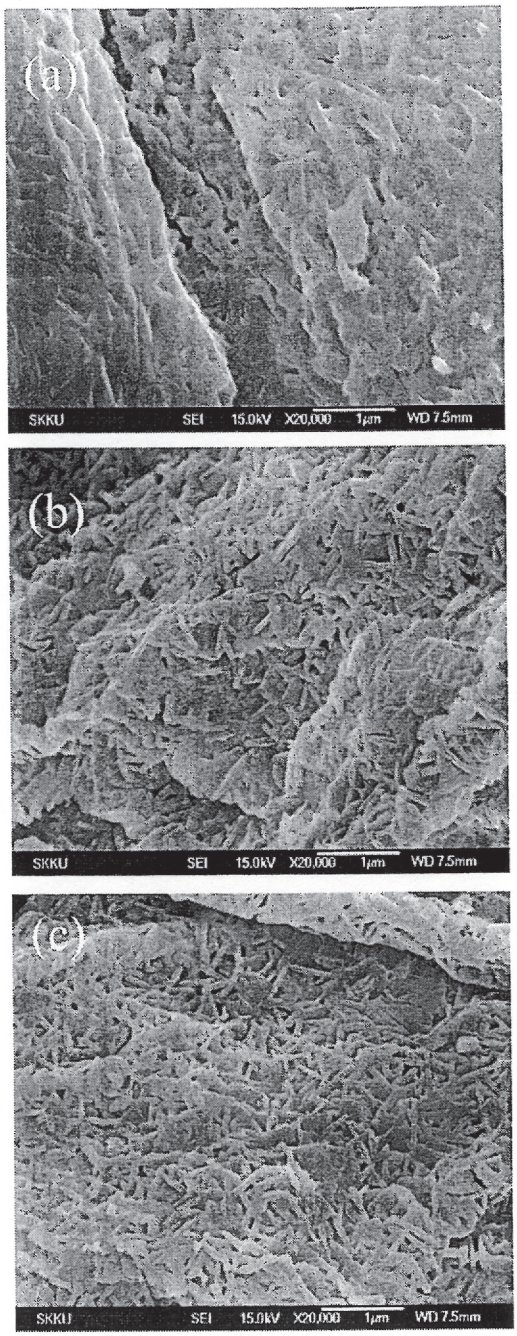

Figure 3.2.2.3. FESEM images of the rod shaped phosphor particles having the compositions of (a) BAM-11, (b) BAM-12 and (c) BAM-13.

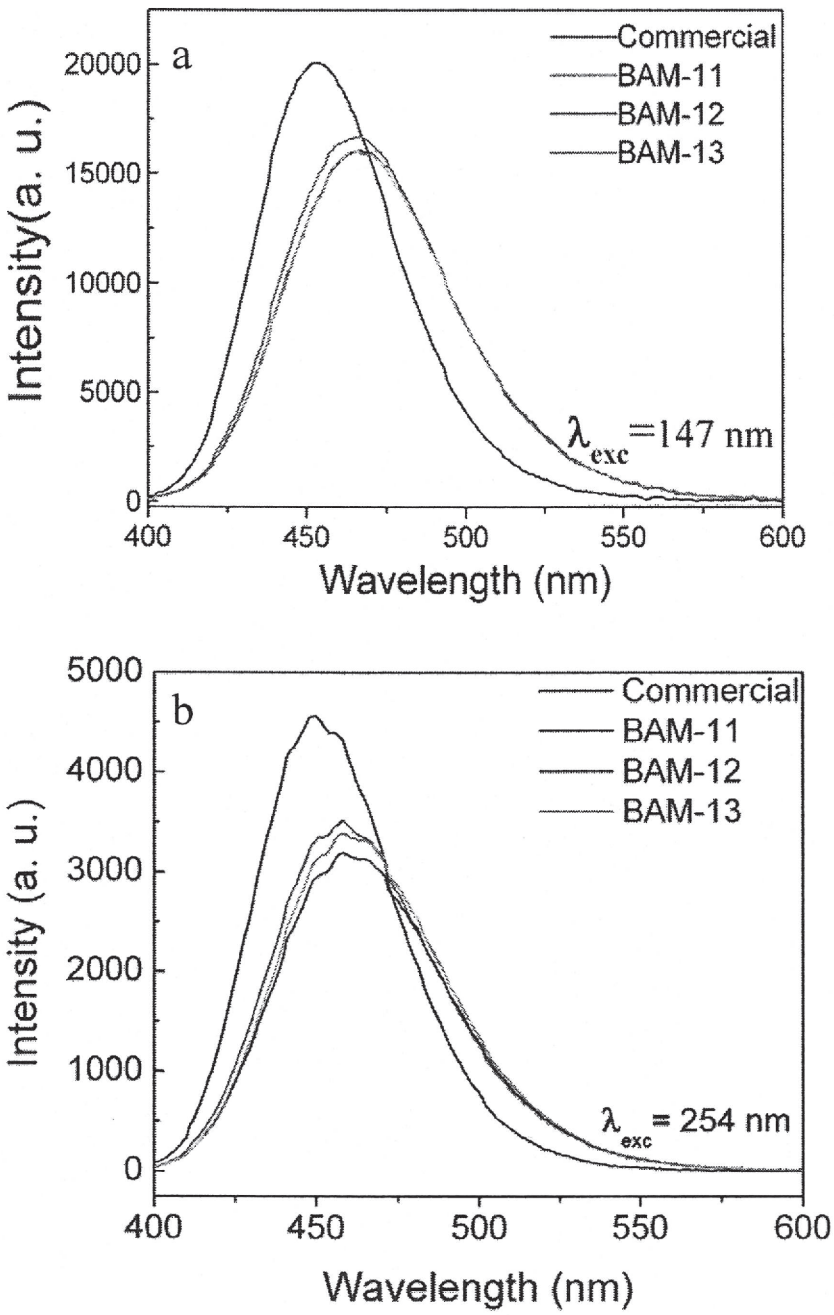

Figure 3.2.2.4. Emission spectrum of BAM specimens excited at (a) 147 nm and (b) 254 nm.

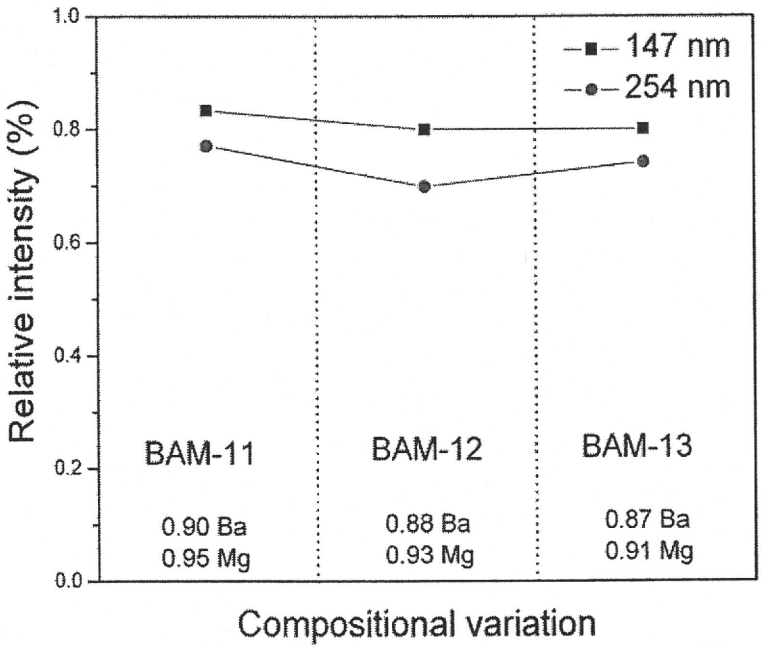

Figure 3.2.2.5. Relative emission intensity of BAM specimens excited at 147 nm and 254 nm wavelength.

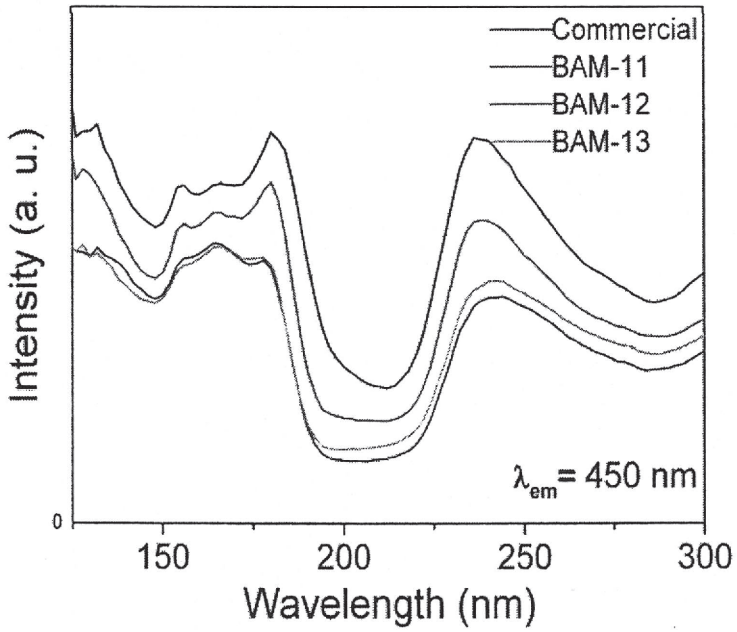

Figure 3.2.2.6. Excitation spectra of BAM samples at room temperature, with the emission maintained at 450 nm.

3.2.3 BAM:Eu nanosized phosphors by polymerizable complex method

Figure 3.2.3.1 shows the XRD patterns of $Ba_{0.87-0.90}Mg_{0.95-0.91}Al_{10}O_{17-17.05}:Eu_{0.05}$ powders prepared by the PC method at 1400 °C for 4 h, confirming formation of $BaMgAl_{10}O_{17}$ registered in JCPDS card no: 260163 . No reflections from extraneous phase were observed. However peak positions exhibits a shift slightly to lower theta degree indicating lattice strain due to smaller particle size.

FESEM images of present sample shows a uniform particle size with average diameter of 50 nm (Figure 3.2.3.2). This sample images was obtained after calcination at 800 °C. When sample was heated in reduction atmosfer to reduce Eu ion at 1400 °C, particle size 2-3 times increased.

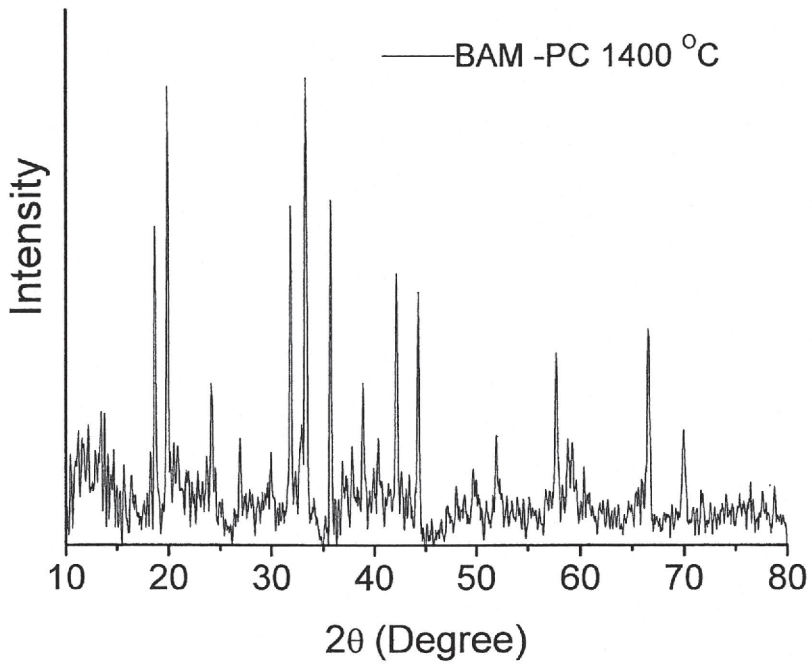

Figure 3.2.3.1. X-ray diffraction pattern of the BAM powder produced by PC method at 1400 °C.

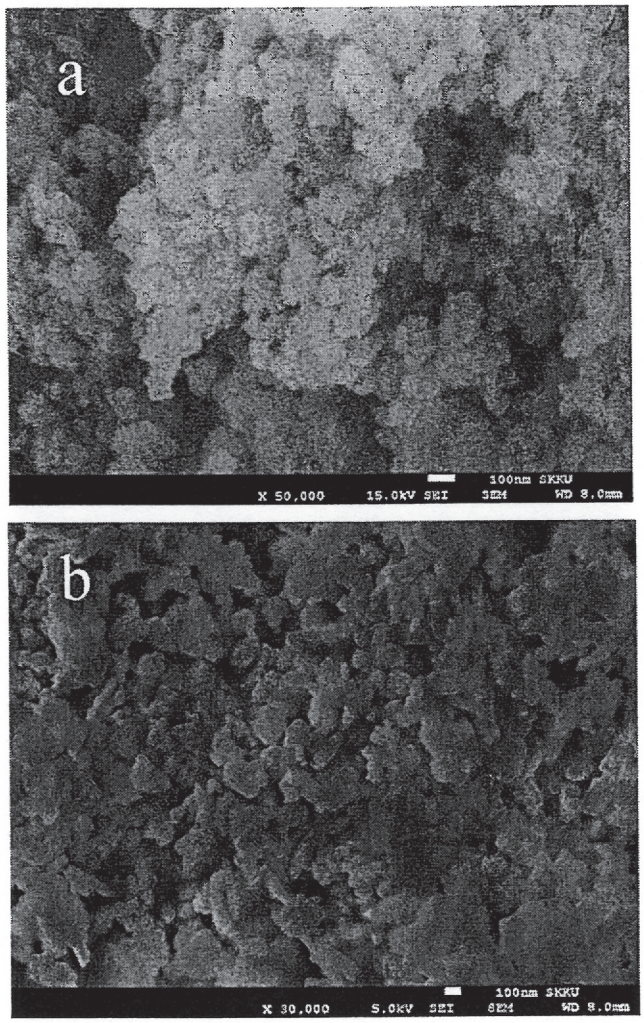

Figure 3.2.3.2. FESEM micrographs of the BAM powder produced by PC method at (a) 800 °C and (b) 1400 °C.

3.2.4 BAM:Eu nanosized phosphors by hydrothermally polymerized gel method

Figure 3.2.4.1. shows the XRD patterns of $Ba_{0.87-0.90}Mg_{0.95-0.91}Al_{10}O_{17-17.05}:Eu_{0.05}$ powders prepared by the PC method at 1400 °C for 4 h, confirming formation of $BaMgAl_{10}O_{17}$ registered in JCPDS card no: 260163 . No reflections from extraneous phase were observed.

FESEM images of present sample shows a spherical morphology with average particle size of 1μm (Figure 3.2.4.2.a.). After heating the present sample at 1400 °C in order to reduce Eu ion, particle size decreased to 500 nm (Figure 3.2.4.2.a.). This implies that heating process lead formation of denser particles. In addition, aggregation was not observed despite high temperature.

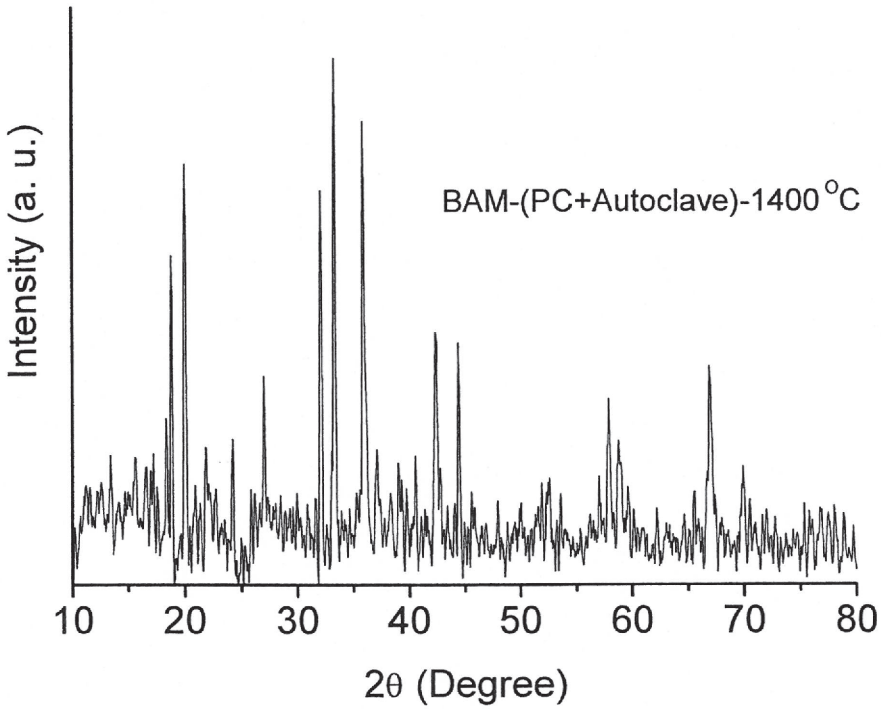

Figure 3.2.4.1. X-ray diffraction pattern of the BAM powder produced by PC combining hydrothermal treatment at 1400 °C.

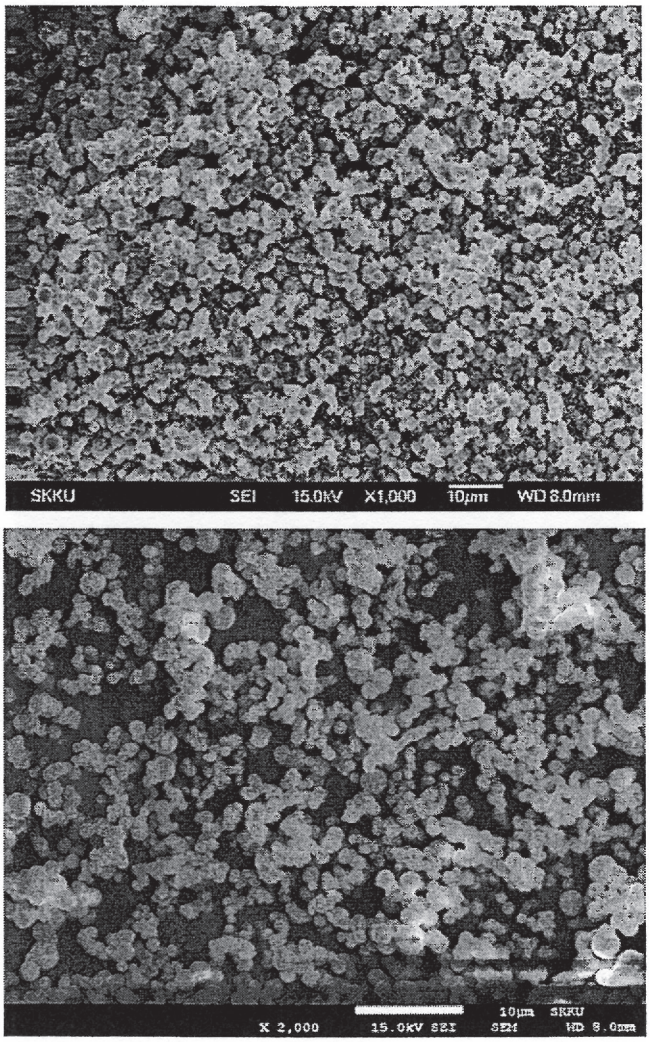

Figure 3.2.4.2. FESEM micrographs of the BAM powder produced by (a) PC method combining hydrothermal treatment (b) after annealing at 1400 °C

3.3 Summary

Blue emitting Eu^{2+} doped barium-magnesium aluminate (BAM) nano-phosphors were synthesized using liquid phase precursor (LPP) method corresponding to $Ba_{0.87-0.90}Mg_{0.91-1.0}Al_{10}O_{17-17.05}:Eu_{0.05}$. The rod shaped phosphor particles ~60 nm in diameter and 400-700 nm in length were obtained. The phosphor particles emission peaks shifted towards a longer wavelength with 80 % luminescence intensity compared with the commercial BAM.

A polymerized complex method invented by Prof. Kakihana was used to support LPP method. We have synthesized BAM nanoparticles with average diameter of 50 nm using prophylene glycol and citric acid. First polymerized gel was produced through the esterification process between prophylene glycol and citric acid. This gel has short length chain compared to cellulose. Therefore we think that, chain length is effective on particle size.

A hydrothermal synthesis of BAM nanoparticles was performed using polymerized gel as a template. The important thing that we performed in here is the use of carboxymethyl cellulose instead of prophylene glycol.

It was found that the prepared particles had a spherical shape and homogenous particle size distribution. After annealing sample at 1400 °C, the morphology of the powders retained and particles size decreased from 1 μm to ~500 nm due to densification.

CHAPTER 4

Surface treatments and functionalization of nanoparticles

Over the last 30 years, the design of new materials on the nanometre scale has been considerable of interest in fundamental science and technology. As the size of materials decreases to the sub micron range, they begin to exhibit interesting electrical, optical, chemical and magnetic properties that are different from their bulk counterparts [41]. In this sense, size controlled synthesis is of key importance, because optimization of the material properties may provide opportunities to increase their areas of application. For example, while single crystal orthovanadates can be applied as a host crystal to solid state lasers, there is also the possibility of some special applications of bio-imaging and biosensors by reducing the crystallite size to the nanoscale [42, 43]. Accordingly, colloidal chemistry presents an effective way of synthesizing materials over a wide size range. However, nanoparticles exhibit a lower luminescence efficiency (~20%) compared to their micron size counterparts due to the increases in structural distortion on the surface with a size reduction [44].

Unlike nanoparticles produced from "bottom-up" approach such as self-assembly and templated synthesis, nanoparticles from mechanical attrition can be produced by a "top down" approach. Such nanoparticles are prepared in a mechanical device, generically referred to as a "mill," in which energy is imparted to a course-grained material to reduce particle size. However, the resulting phosphor materials exhibit weak luminescence intensity as the milling process leads the formation of defects on the surface. In the case of luminescent nanoparticles, the surface plays an important role in energy transfer and defects act as a sink for the radiative energy transitions by producing levels in the forbidden gap. Generally, these states are closely spaced to local levels that reduce the efficiency of the phosphors enhancing the non-radiative transitions [45].

Many attempts have been made to compensate for this large loss of intensity and significant increase in quantum yield was observed after either capping with a silica shell or functionalization with organic surfactants [46-48].The aim of this study was to purify the surface of $Y(P,V)O_4$ with an alkali solution treatment, which is used widely in ceramic applications to improve the surface states. Abrupt crystal growth was observed at room temperature with a ~23% improvement in luminescence intensity. This interesting result motivated us to clarify the mechanism of luminescence enhancement of $Y(P,V)O_4$:Eu nanoparticles when treated with an alkali solution.

4.1 Experimental

4.1.1 Milling of BAM:Eu nanosized phosphors and surface capping with organic functional group

Herein, nanoparticles of BAM:Eu^{2+} phosphor were prepared by ball-milling process. Formerly, micron-sized BAM:Eu^{2+} phosphor particles were synthesized by LPP method at 1450 °C under a 5% H_2/N_2 atmosphere, as described elsewhere [50]. A mixture of Φ1.5 and 3mm glass beads, phosphor powder and deionized water with a beads/powder/water weight ratio of 1:0.03:1 were sealed in a plastic vial. The vial was rotated at a speed of 300 rpm for 15 h. Two different milling conditions were selected. In the case of first condition (A), 0.2% dispersant agent (Flowlen G700, Kyoeisha chemical co, ltd.) containing deionized water was used to functionalize the particle surface. The other sample (B) was milled only in deionized water. After separating the glass beads, the milky powder solutions were poured into a centrifuge tubes and centrifuged at a speed of 4000 rpm for 10 min. In order to purify the particle surface, half of sample S2 was dispersed in a 5% KOH solution, stirred for 10 min and centrifuged again (C). The resulting precipitates were dried at 80 °C for one day.

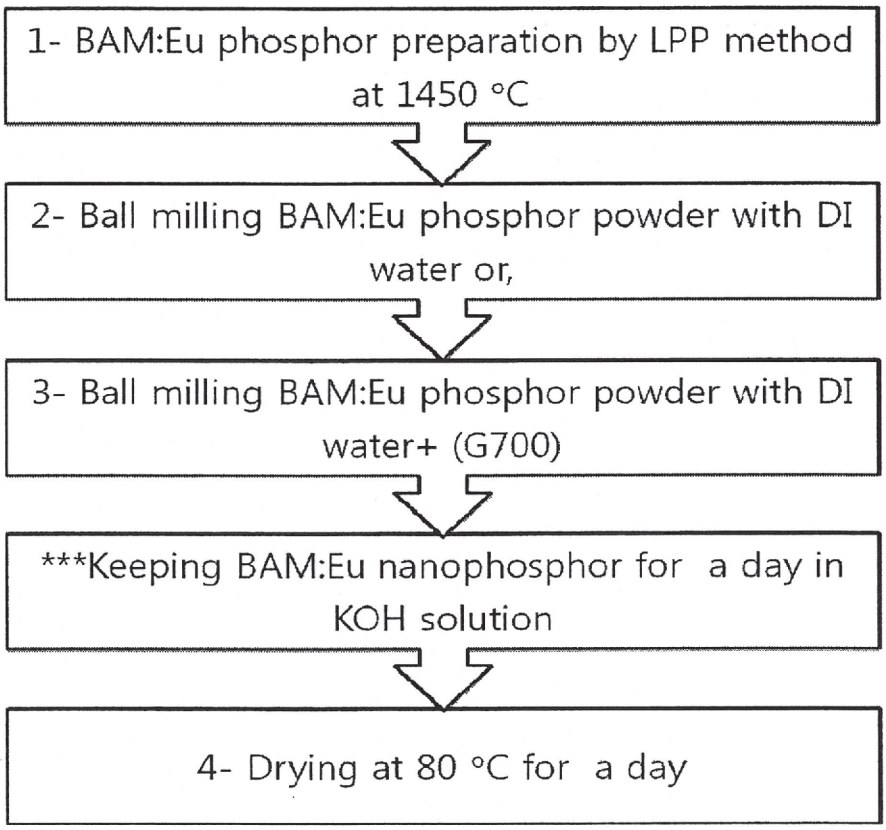

Figure 4.1.1.1 Flowchart for milling process and surface treatments

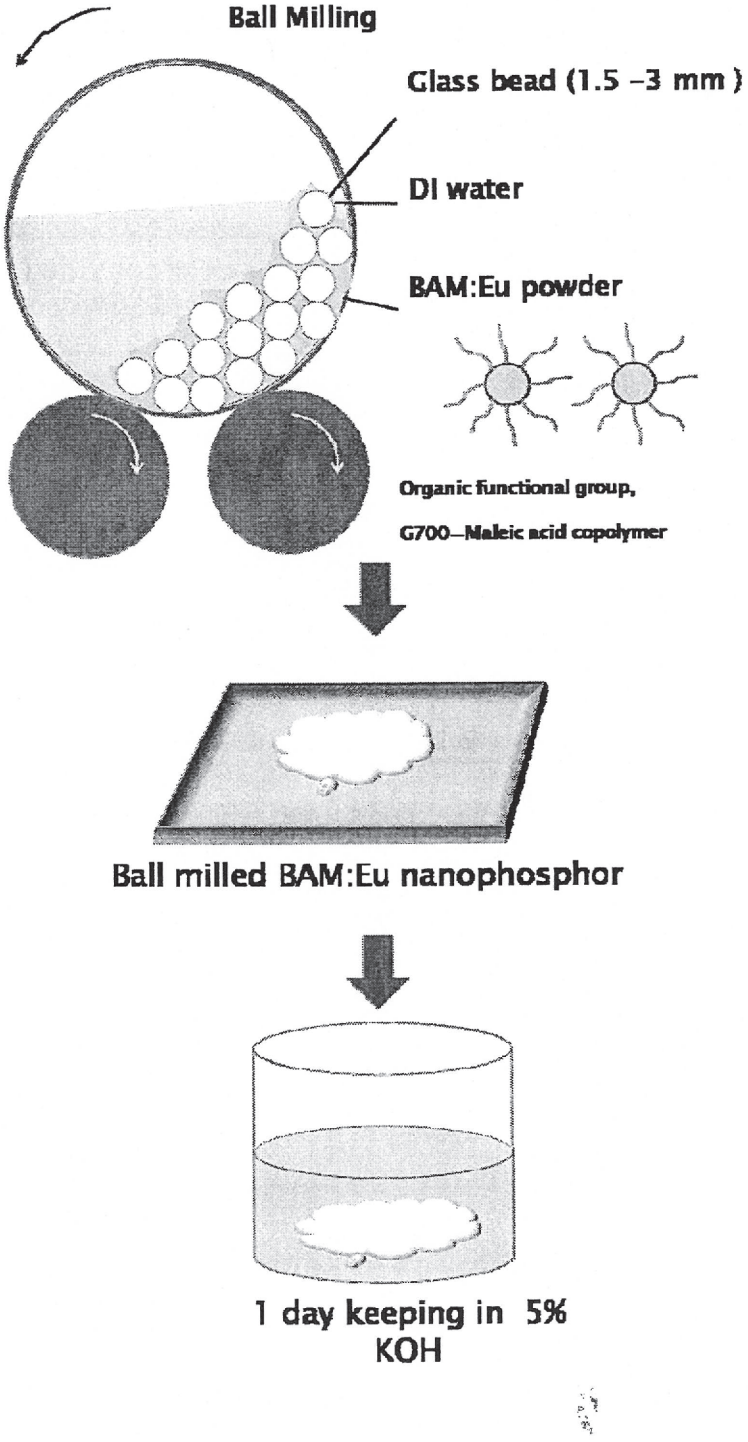

Figure 4.1.1.2 Schematic description of milling process and surface treatments.

4.1.2 Surface treatment of YPV:Eu nanosized phosphor

The cellulose pulp was used to synthesize $Y_xP_{0.70}V_{0.50}O_4:Eu_{0.1}$ (x=0.96, 0.99, 1.05) nanophosphors using the liquid phase precursor (LPP) method [18]. The raw materials ($VO(SO_3)\cdot nH_2O$, ≥ 99.99 %), phosphoric acid (H_3PO_4, 99.99 %), yttrium chloride ($YCl_3\cdot 6H_2O$, ≥ 99.99 %) and europium chloride ($EuCl_3\cdot 6H_2O$, ≥ 99.99 %) were dissolved in deionized water.

Aqueous solutions of these metal salts were mixed corresponding to a molar ratio of $Y_xP_{0.70}V_{0.50}O_4:Eu_{0.1}$ (x=0.96, 0.99, 1.05) and 100 g of cellulose pulp was impregnated into 100 ml of the resulting mixture solution. The impregnated pulp was dried at 80 °C in a dry oven, and calcined at 800 °C for two hours to remove the cellulose template. Subsequently, the calcined powder was heated from room temperature to 1150 °C at a heating rate of 200 °C. h^{-1} in air. The resulting as-grown phosphor nanoparticles were dispersed in a 5% KOH solution and kept for one day at room temperature.

The emission spectrum was measured at room temperature using a xenon lamp (500 W) as the source of the PL spectrophotometer (PLE/PL Drasa PRO 5300, Korea) over the range, 350–700 nm, and 220–380 nm. Powder X-ray diffraction (XRD, Cu Kα, 30 kV, 100 mA, Rigaku) was used to determine the crystalline phases of the synthesized samples. The surface morphology and crystallinity of the resulting particles were observed by scanning electron microscopy (FESEM, XL-30, Philips) and high resolution transmission electron microscopy (HR-TEM, JEOL 300kV). The elemental content was analyzed by inductively coupled plasma emission spectrometer (Perkin-Elmer Optima 5300 DV ICP-OES). Fourier transform infrared (FTIR) spectra were collected in the mid-IR range (4000−500 cm−1) with a spectrophotometer (Nicolet 200-FTIR) in absorbance mode to deduce functionality of surface with organic residue.

4.2 Results and discussions

4.2.1 Milling effect and enhanced luminescence property of BAM:Eu

Figure 4.2.1.1 shows the XRD patterns of the BAM:Eu^{2+} powder samples prepared by LPP method before and after ball-milling. All the main diffraction peaks of the samples were well indexed to hexagonal structured $BaMgAl_{10}O_{17}$ according to the JCPDS card (no. 26-0163). The maximum peak intensity of the crude sample (Fig. 4.2.1.1.1 (a) at 33.3° 2θ was slightly narrower than that of the ball-milled samples (Fig. 4.2.1.1 (b-d)), indicating a larger primary particle size. In the case of the dispersant agent containing sample (Fig. 4.2.1.1 (d) no extraneous phase was detected because amount of dispersant was very small and the unattached polymers were probably removed after centrifugation.

Figure 4.2.1.2 shows FESEM images of the BAM Eu^{2+} samples. Fig. 4.2.1.2 (a) presents the crude BAM:Eu^{2+} powder synthesized using the LPP method. The synthesis resulted in highly aggregated rod shaped particles. After ball-milling, the particles size decreased to the sub-micron range with an irregular morphology (Fig. 4.2.1.2 (b-d). The state of agglomeration and size distribution were deduced from electrophoretic light scattering analyses (Figure 4.2.1.3) of BAM:Eu^{2+} powders dispersed in deionised water. The mean particle size of the crude sample was approximately 2.3μm with an inhomogeneous size distribution profile, which was 2-3 times larger than FESEM images of same sample (Figure 4.2.1.2 (a)). After ball milling of this crude sample for 15h, the mean particle size decreased to 442.5 nm in diameter with a broad size distribution. This was also 2-3 times larger than FESEM images of same sample (Figure 4.2.1.2 (b) indicating aggregation problem. In order to improve surface state of ball milled sample, KOH solution treatment and surface modification with organic surfactant was applied, individually. In the case of KOH solution treatment, particle size analyses showed an increase in particle size from 442.5 to 3472.6 nm in diameter due to aggregation mediated particle growth which was caused by inter particle

interactions through hydrogen bondings [49]. The organic surfactant (Flowlen G700, Kyoeisha chemical co, ltd.) was used to modify the particle surface to enhance the luminescence efficiency and good dispersibility. In the case of dispersion agent-containing sample exhibited several size distributions with a mean particle size of 705.6 nm. This value seems reasonable since an increase in particle size is expected after modification of particle surface with organic surfactant. However, observed several size distributions above than micron range are a sign of aggregation problems. It was reported that when submicron-sized particles are exposed to polymeric agents, the dispersions become unsuitable because the molecular size of the polymer is comparable to the size of the particles, leading to particle–particle bridging that may result in aggregation [50]. Therefore, further experiments are reguired to optimize the conditions related to the homogenous size distribution and good dispersibility.

The surface state of the particles with regard to the functionality of the organic surfactant and hydrogen bonding were analysed by Fourier transform infrared (FTIR) spectroscopy (Figure 4.2.1.4). No peaks related to organic functional groups were observed in the ball milled sample (Fig. 4.2.1.4 (a)). After KOH solution treatment, this sample exhibited a broad band peaking at 1365 cm^{-1} (Figure 4.2.1.4 (b)). The origin of this peak was not clear because no organic was used. However, O-H stretching vibration due to hydroxyl group funtionalization at around 3340 cm^{-1} was observed with a negligible intensity. On the other hand, C=O, C-H and C–O stretching modes belonging to carboxylic groups appeared at 1740, 1365 and 1218 cm-1 in the dispersion agent containing sample (Figure 4.2.1.4 (c)) agreeing well the functionalization of particles surface with organic surfactant [51].

Figure 4.2.1.5 shows the emission spectrum (λ_{exc}= 254 nm) of the BAM:Eu^{2+} powder before and after the milling process. The emission spectra exhibited a broad band at 458 nm, which was assigned to the transitions of Eu^{2+} ions from the $4f^6 5d$ level to the $4f^7$ ground state

[52]. The crude sample emission intensity decreased sharply after the milling process due to the large surface area to volume ratio and the formation of significant amount of defects.

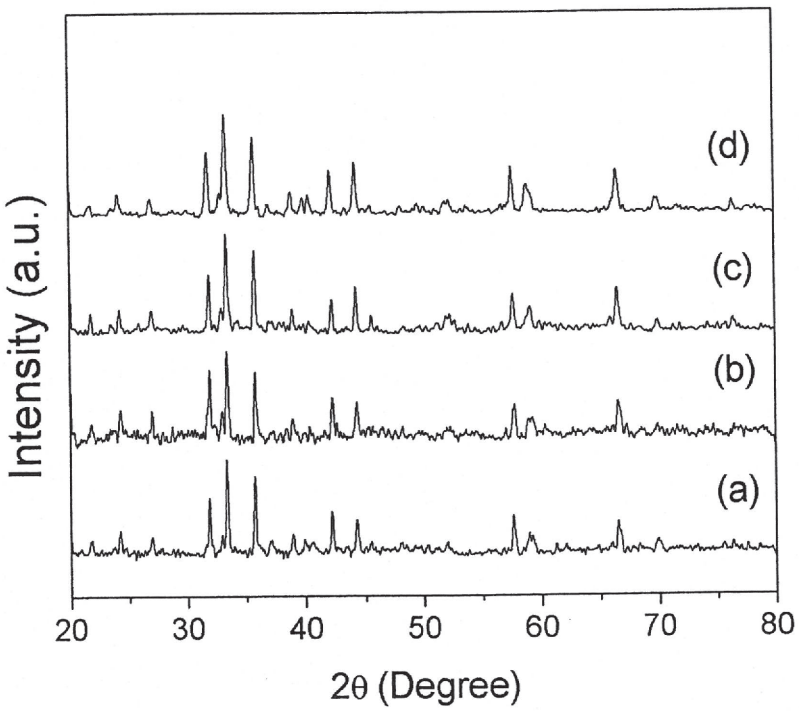

Figure 4.2.1.1. XRD patterns of (a) crude and (b-d) ball- milled BAM:Eu^{2+} samples .

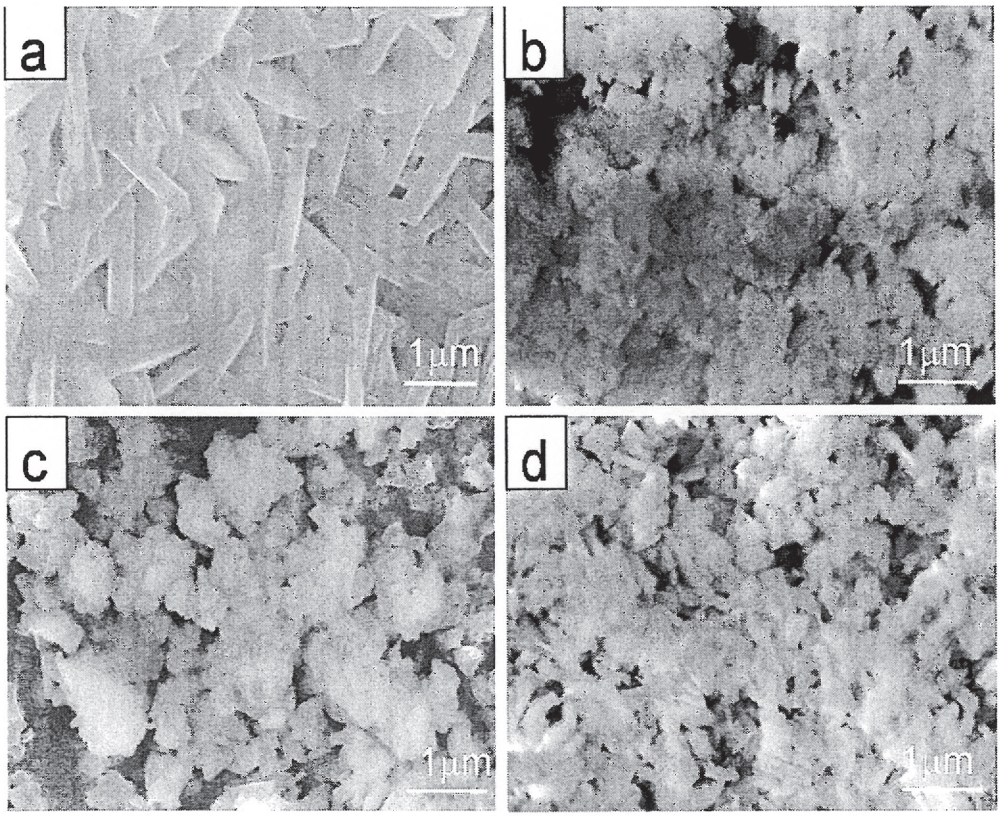

Figure 4.2.1.2. FESEM images of the BAM:Eu^{2+} samples (a) before and (b-d) after ball-milling with deionised water. After milling, the sample surface was purified with a 5% KOH solution, as shown in fig.2 (c). Figure 2 (d) shows FESEM images of the sample milled with the dispersant agent (Flowlen G700, Kyoeisha chemical co, ltd.).

.

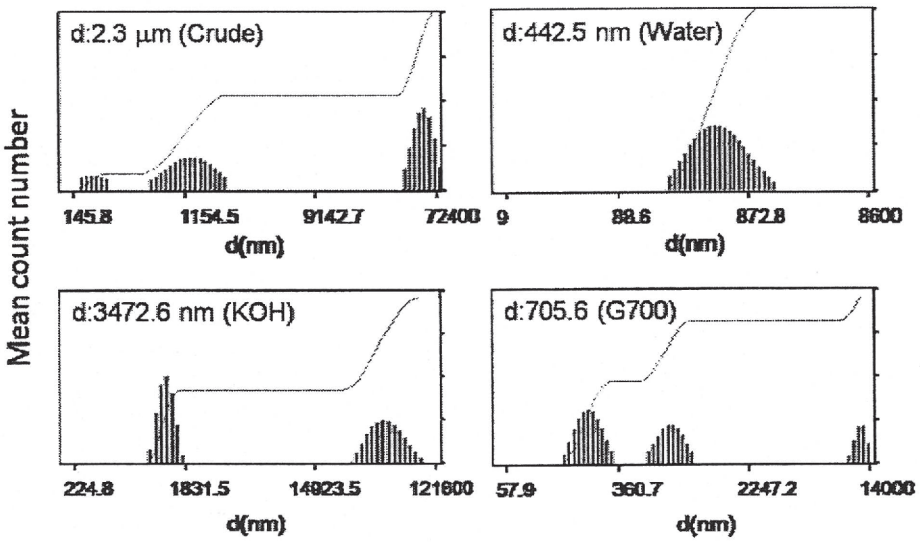

Figure 4.2.1.3. Electrophoretic light scattered (ELS) size distribution analyses of the crude and ball-milled samples.

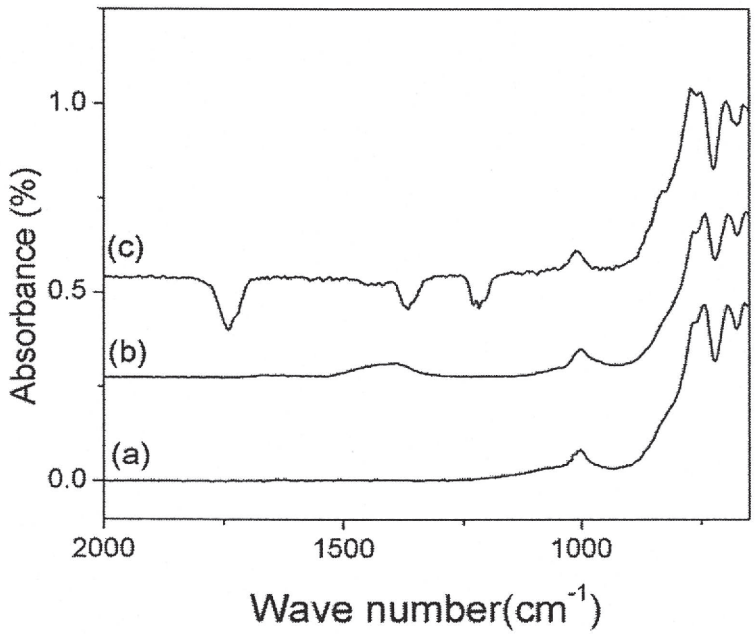

Figure 4.2.1.4. FTIR analysis of the ball-milled BAM:Eu^{2+} samples. Fig. 4 (a) absorbance spectrum of the ball-milled sample with (a) deionised water, (b) KOH treated sample and (c) dispersion agent containing sample.

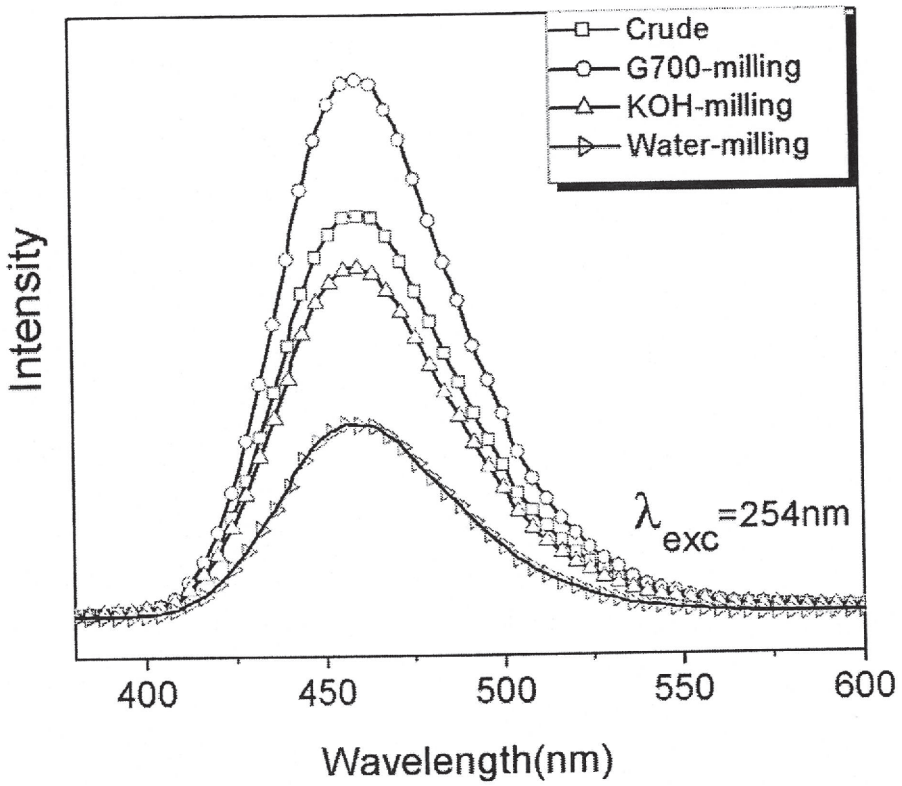

Figure 4.2.1.5. The photoluminescence emission spectrum (λ_{exc}= 254 nm) of the BAM:Eu^{2+} samples.

4.2.2 Surface treatment and luminescence property of YPV:Eu nanosized phosphors

The XRD patterns of the $Y_xP_{0.7}V_{0.5}O_4:Eu^{3+}$ (x=0.96, 0.99, and 1.05) samples, as shown in figure 4.2.2.1, was measured before and after the KOH solution treatment. All the recorded peaks were between the standard YVO_4 (JCPDS, 72–0274) and YPO_4 (JCPDS, 11–0254) pattern, which agree well with the Vegard law [15]. Before the treatment (for sample S1, S2 and S3), all diffraction peaks narrowed with increasing Y concentration. After treatment, no extraneous phase could be detected that can show the dissolution of smaller YPV:Eu particles in KOH solution and there was no clear difference in the peak position, width and intensity.

The particle size and morphology of the $Y_xP_{0.7}V_{0.5}O_4:Eu^{3+}$ (x=0.96, 0.99, and 1.05) samples before and after the 5% KOH solution treatment were examined by FESEM (Figure 4.2.2.2). The samples named S1, S2, and S3 correspond to 0.96, 0.99, and 1.05 mol percent of Y. The as grown particles had a round shaped with sizes increasing with increasing Y concentration (Figure 4.2.2.2 (a, b and c). This illustrates the lattice expansion in $Y_xP_{0.7}V_{0.5}O_4:Eu^{3+}$ (x=0.96, 0.99, and 1.05) samples as regard to Y^{3+} concentration [20]. After dispersing particles in a KOH solution treatment, the samples were named S1-KOH, S2-KOH, and S3-KOH, and abrupt crystal growth was observed at room temperature from ~50 to ~300 nm, ~150 to ~300 nm and ~300 to ~500 nm, respectively (Figure 4.2.2.2 (a-f)). This interesting growth phenomena at room temperature seemed to be originated from Ostwald ripening effect at a first glance. However, ICP elemental analyses of powder mixed KOH solution showed YPV:Eu sample was insoluble since no Eu^{3+}, Y^{3+}, P^{5+} and V^{5+} ions regarding to YPV:Eu compound were detected (Table 4.2.2.1). This implied that the growth mechanism of the YPV:Eu nanocrystals in a KOH solution did not fallow Ostwald ripening process in which molecules on the surface of a small particle tend to detach and diffuse through solution and then attach to the surface of larger particle. Even if there was some dissolution, according to Ropp and Carroll [53], the temperature should be high enough for

the recrystallization of orthovanadates. An alternative approach, so-called aggregation-mediated crystallization, can occur through interactions, such as hydrogen bonding, van der walls or electrostatic interactions between the preformed nanoparticles [54, 55]. Accordingly, S. Erdei et.al [56] developed a method for the synthesis of YVO_4 powder. In their report, the particles were first hydrolyzed during the collisions and a partially ionized surface of each particle resulted in hetero-aggregation due to electrostatic interactions. Afterwards, this hetero-aggregated colloid underwent a further reaction to form orthovanadate when excess hydrolysis was accessed under high pH conditions. In the case of the current sample crystal growth was assumed to be originated due to the electrostatic interactions of colloidal particles. The KOH solution is believed to act as a hydrolyzing agent and each particle was partially ionized. Subsequently, the particles flocculate due to electrostatic interactions, which results in rapid crystal growth.

In order to understand effect of KOH solution on the surface state of nanoparticles, a comparative surface analysis of sample S1 before and after KOH solution treatment was made by FTIR spectroscopy (Figure 4.2.2.3). Both samples exhibited two strong bands extending between 700–950 cm^{-1} and 950-1200 cm^{-1}, correspond to Y-O and V-O stretching. In addition to these two bands, small peaks were observed at 1402 and 1531 cm^{-1} due to symmetric and asymmetric vibrations of carboxylate group for sample S1 [57]. These two bands vanished after treading sample with KOH solution, suggesting that a considerable quantity of organic residue presented on the surface of as-grown nanoparticles was removed.

In addition to FTIR spectroscopy the surface state of sample S1 before and after the KOH solution treatment was examined by HR-TEM (Figure Figure 4.2.2.4 (a, b). The residue on the surface, as indicated by arrow in Figure 4.a, was removed by the KOH solution treatment, and the surface became quite smooth. In addition, SAED pattern of sample S1 confirmed the smoothness by indicating disappearance of additional diffraction spots which means the

removal of a layered structure near the surface (inset of Figure Figure 4.2.2.4 (b)). This suggests that the KOH solution treatment both purifies the surface and causes smoothing.

Figure 4.2.2.5 shows that the excitation (λ_{em}= 618 nm) and emission spectrum (λ_{exc}= 254 nm) of the $Y_xP_{0.7}V_{0.5}O_4:Eu^{3+}$ powder samples before the KOH treatment. In this figure, the luminescence intensities were normalized with respect to the micron sized commercial product. The excitation spectrum exhibited broad band extending between 225-350 nm and weak bands in the longer wavelength region (inset figure 4.2.2.5). The former band was ascribed to a charge transfer from the oxygen ligands to the central vanadium atom insides the VO_4^{3-} group ions, and the latter bands peaking at 381, 395, and 400nm originated due to f-f transitions of Eu^{3+} ions. It has been reported that the multiphonon relaxation by VO_4^{3-} is not able to bridge gaps between higher energy levels ($^5D_1$, $^5D_2$, $^5D_3$) to $^5D_0$ level resulting weak emissions from these levels [58]. The positions of charge transfer band sligthly shifted towards longer wavelength direction as increasing Y concentration except for sample S3. The reason for this may be due to lattice disorder and variation of V-O avarage bond length as a result of large ionic radii of Y atom [59]. On the other hand, compared to the commercial sample there must be a difference in peak position. Because, the V–O average distances for smaller nanoparticles are longer than for larger nanoparticles, and the excitation energy required is higher for $V^{+5}O_n^{-2n} \rightarrow V^{+4}O_n^{-2n+1}$. However, excitation peak intensity of commercial sample interestingly lies a position same with the our samples eventhough its particle size one order larger. This implies the particle size may not have influence on the V–O average bonding length [60]. The emission spectra consisted of three peaks assigned to $^5D_0$–$^7F_1$ (magnetic dipole transition) and $^5D_0$–$^7F_{2,4}$ (forced electric dipole transitions). The absence of inversion symmetry at the Eu^{3+} lattice site (D_{2d} symmetry) resulted in strong luminescence intensity at 621 nm through $^5D_0$–$^7F_2$ transitions [61, 62]. The integrated

emission intensities of the YPV:Eu samples at 621 nm showed an increase in PL intensity with increasing Y concentration. After the solution treatment luminescence intensity of $^5D_0$–$^7F_2$ transitions further improved and ~5 and ~23% increases were obtained for samples S1 and S2. However ~9% luminescence intensity loss was observed for sample S3 (Table 4.2.2.2). Based on TEM and FTIR analyses an improvement in luminescence intensity after alkali solution treatment can be described by the fallowing: the removal of residue may reduce the number of non-radiative transitions and smoothing of the surface may leads to a decrease in the scattering of UV light from the surface. In the case of sample S3 the reason of intensity loss was not clear. However, the evaluation of intensity ratio of hypersensitive transitions may bring some insigth for understanding the energy transfer mechanism. A direct relationship was reported between the structural distortion and the ratios of the $^5D_0$–$^7F_2$ and $^5D_0$–$^7F_1$ integrated transition intensities, so-called asymmetry [63]. Table 4.2.2.2. shows the emission intensity of all samples at 595 and 621 nm corresponding to the $^5D_0$–$^7F_1$ and $^5D_0$–$^7F_2$ transitions and the calculated asymmetry ratios. Considering higher surface/volume ratios in nanocrystals, more Eu^{3+} ions locate on the surface or near the surface with disorder compared to interior Eu^{3+} ions. These reasons lead to a high luminescence intensity and the asymmetry for initial nanoparticles. When nanoparticles grow, which reduces the Eu^{3+} ions on the surface.Therefore, it is expected that asymmetry ratio should decrease after the KOH treatment because the growing crystal recover the structural distortion near the surface. However, after the solution treatment, the asymmetry ratio is sligthly larger within this growing shell layer. This implies that this growing layer is formed due to aggregation of smaller particles not due to better crystallization. This is consistent with the appearance of a higher luminescence intensity of the $^5D_0$–$^7F_2$ transition. The reason of the intensity loss for sample S3 may be originated from hard aggregation which is known as luminescence

quencher due to formation of traps near the surface. It can be inferred from these results that the asymmetry is quite effective on the luminescence efficiency.

This study examined the interesting crystal growth mechanism and enhanced luminescence property of $Y_xV_{0.70}P_{0.50}O_4$ (x=0.96, 0.99, 1.05) nanophosphors. A 5% KOH solution was used to purify the surface of the as grown nanoparticles. Interestingly, significant grain growth occurred at room temperature due to partial electrostatic interactions between the partially ionized surface of the nanoparticles. After the solution treatment, a higher emission intensity of Eu^{3+} ions corresponding to the $^5D_0-^7F_2$ transition was observed due to purification of surface from organic residue and high asymmetry of Eu^{3+} ion sites within the growing shell layer.

Table 4.2.2.1 *ICP analyses of YPV:Eu powder. The samples were analyzed after 24 h and after sedimentation in the 5% KOH solution.*

Concentration(ppm)	Y	P	V	Eu
24 h	Not detected	2.4	3.7	Not detected

Table 4.2.2.2 The emission intensity of all samples at 595 and 621 nm corresponding to $^5D_0$–$^7F_1$ and $^5D_0$–$^7F_2$ transitions, calculated asymmetry ratios and improvement in emission efficiency.

	$^5D_0$–$^7F_1$ (595 nm)	$^5D_0$–$^7F_2$ (621 nm)	$^5D_0$–$^7F_2$ / $^5D_0$–$^7F_1$	Efficiency increments
S1	1007	4014	3.98	+5.2%
S1-KOH	1003	4224	4.21	
S2	1066	4248	3.98	+23.4%
S2-KOH	1302	5550	4.26	
S3	1346	5534	4.11	-9.3%
S3-KOH	1237	5018	4.05	

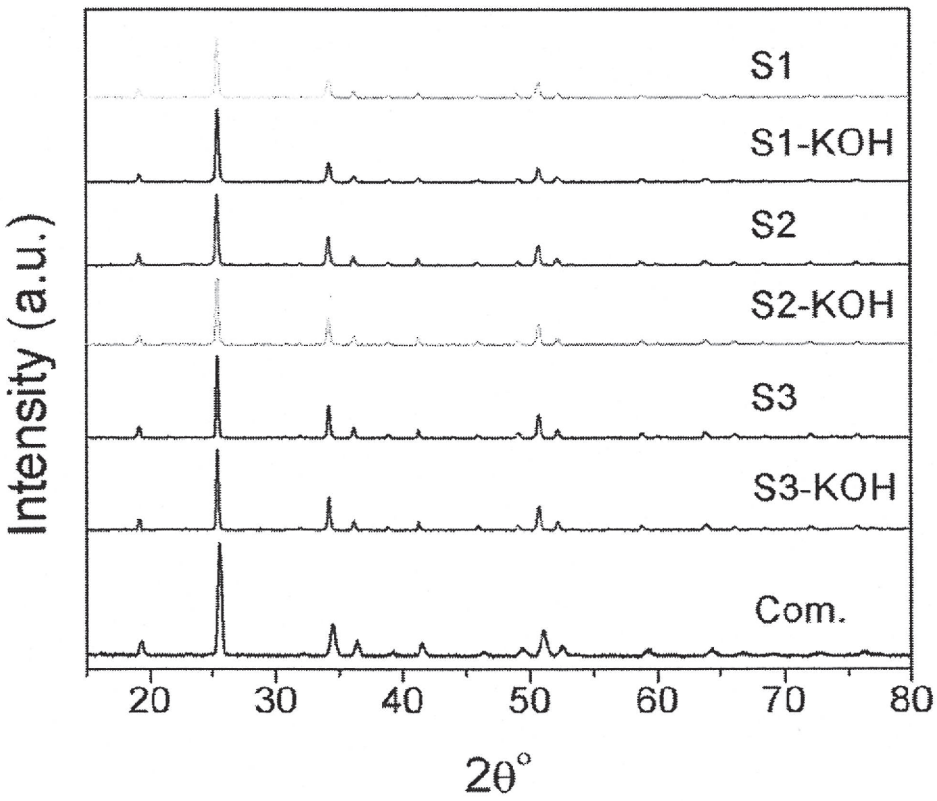

Figure 4.2.2.1 The XRD patterns of $Y_xP_{0.7}V_{0.5}O_4:Eu^{3+}$ (x=0.96, 0.99, and 1.05) before and after the 5% KOH solution treatment. A commercial product is used as a reference.

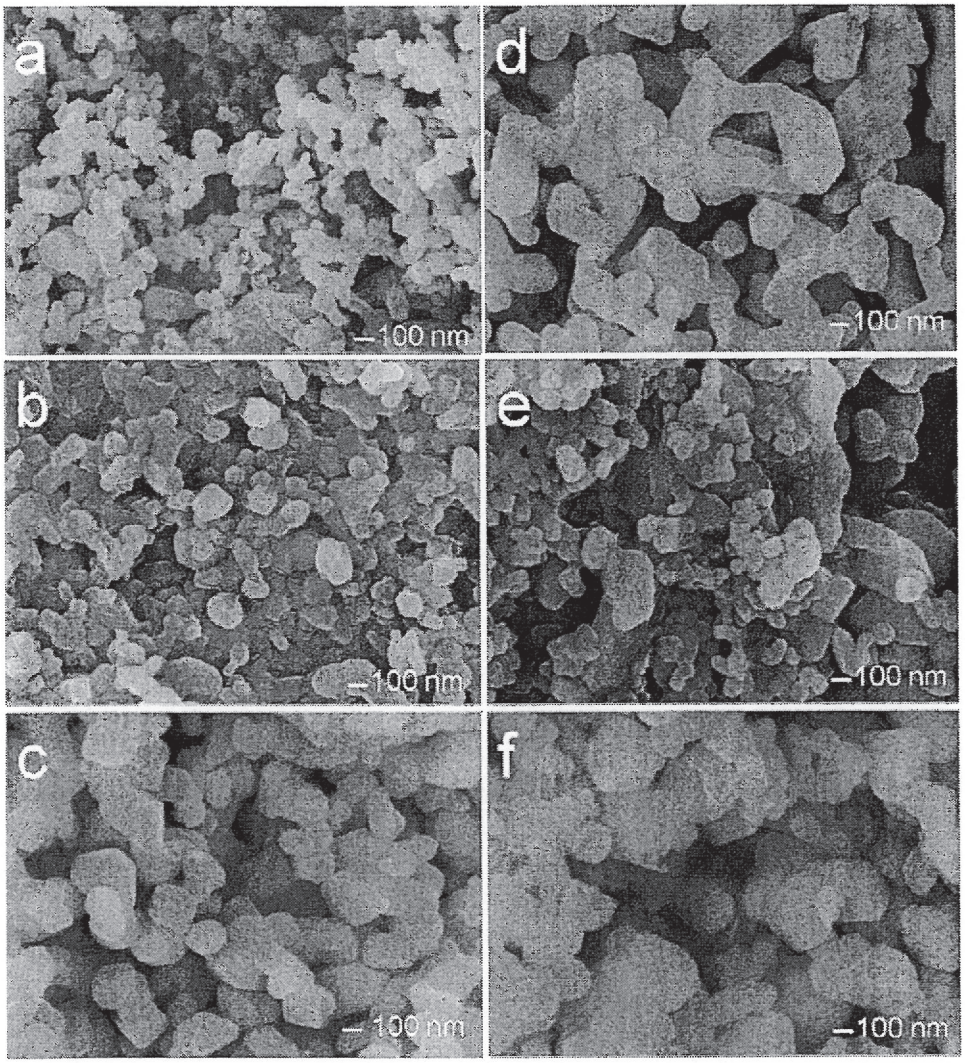

Figure 4.2.2.2 FE-SEM images of $Y_xP_{0.7}V_{0.5}O_4:Eu^{3+}$ samples. The yttrium concentration increased from the upper to lower part (a) x=0.96, (b) x=0.99 and (c) x=1.05 and the right column shows images of particles after KOH solution treatment (d), (e), and (f).

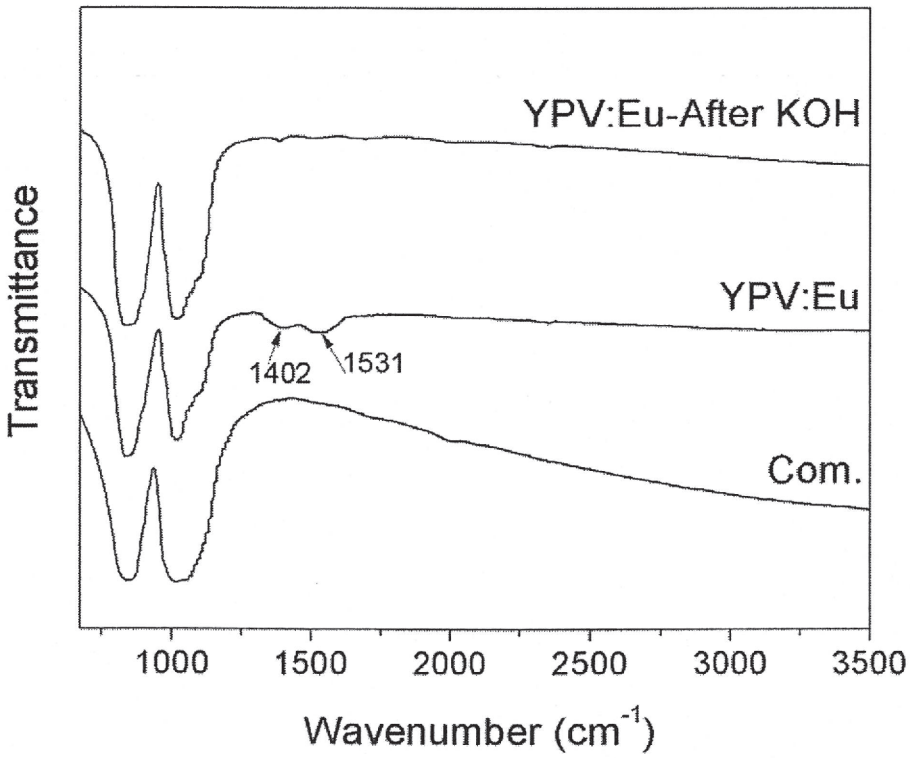

Figure 4.2.2.3 FTIR spectrum of $Y_{0.99}P_{0.7}V_{0.5}O_4:Eu^{3+}$ samples (a) before, and (b) after KOH treatment.

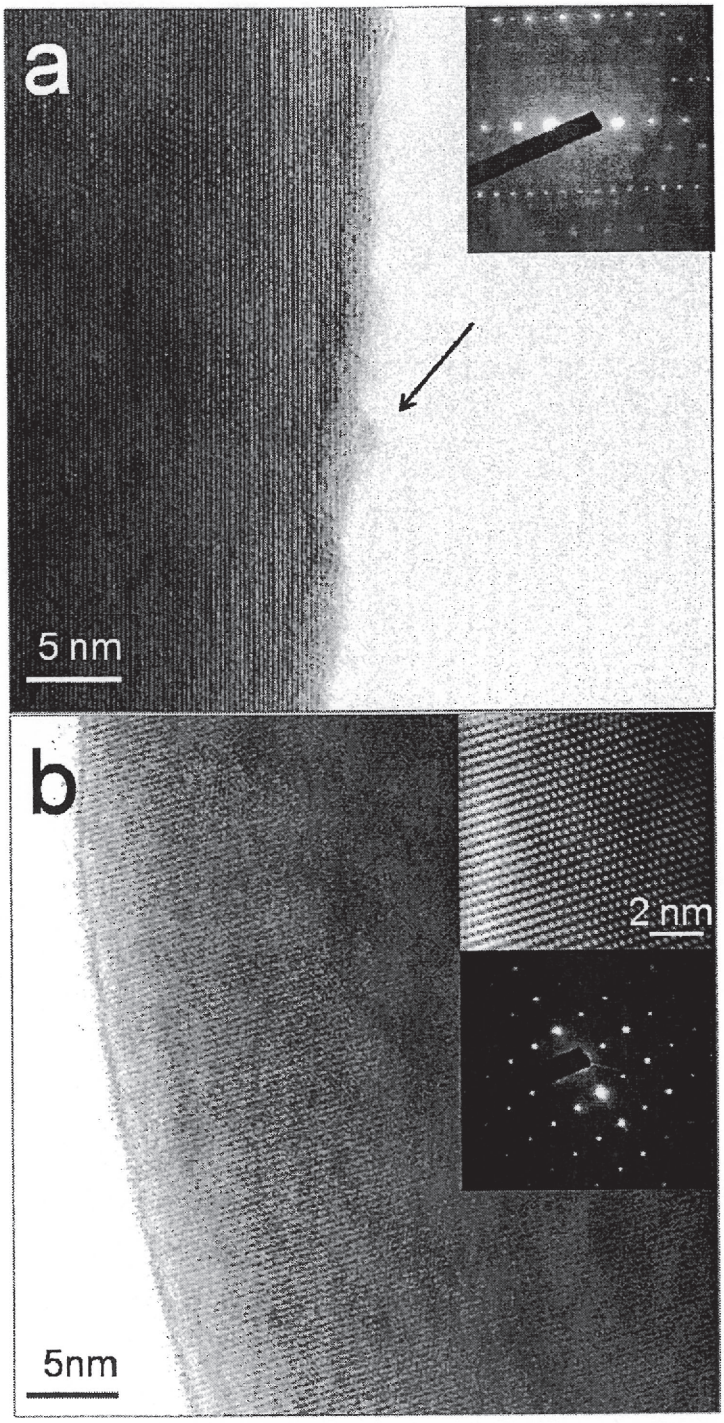

Figure 4.2.2.4 HR-TEM images of $Y_xP_{0.7}V_{0.5}O_4:Eu^{3+}$ samples (a) before, and (b) after KOH treatment. SAED pattern is given in the inset.

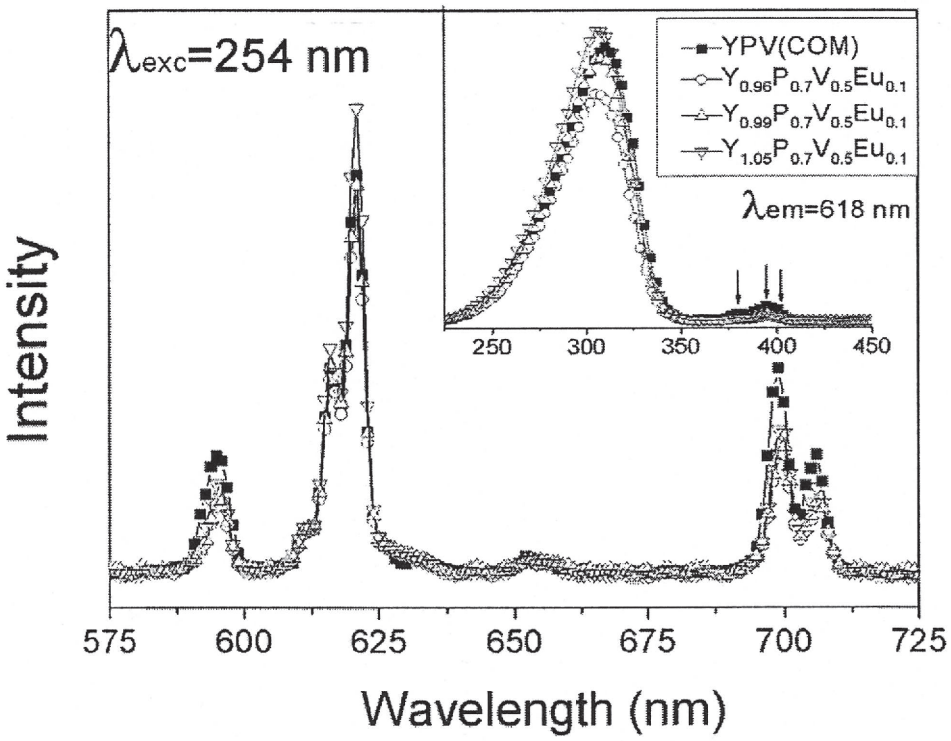

Figure 4.2.2.5 The emission spectrum (λ_{exc}= 254 nm) of $Y_xP_{0.7}V_{0.5}O_4:Eu^{3+}$ powder after 5% KOH solution treatment.

CHAPTER 5. Conclusions

In this dissertation, we intend to synthesis of high efficient blue emitting BAM:Eu and red emitting $Y(V,P)O_4$:Eu nanophosphors by using template based synthesis methods. Firstly, LPP method was introduced and highly efficient $Y_{0.99}P_{0.70}V_{0.50}O_4:Eu_{0.1}$ phosphor particles, ~200 nm in size, were synthesized at 1150°C using cellulose pulp. Strong $^5D_0-^7F_2$ emission of Eu^{3+} ions was observed at 621 nm, and its intensity was ~100.5% of the commercial product. The comparable asymmetry ratios (R) and the absence of line broadening on the luminescence spectrum indicated less structural distortion and high crystallinity of the present sample. In addition to the photoluminescence spectrum, HRTEM demonstrated perfect crystallinity with clear lattice fringes.

Blue emitting Eu^{2+} doped barium-magnesium aluminate (BAM) nano-phosphors were synthesized using LPP method corresponding to $Ba_{0.87-0.90}Mg_{0.91-1.0}Al_{10}O_{17-17.05}:Eu_{0.05}$. The rod shaped phosphor particles ~60 nm in diameter and 400-700 nm in length were obtained. The phosphor particles exhibited 80 % luminescence intensity compared with the larger size commercial BAM and luminescence peak positions shifted towards a longer wavelength (~465 nm) due to compositional difference. PL emission spectra excited at 147 and 254 nm revealed that this shift and broad band was not related to multiple locations of Eu^{2+} ions.

Despite the high efficiency, BAM sample produced by LPP method exhibited aggregation problem. In order to solve this problem, various methods were also performed. A polymerized complex method invented by Prof. Kakihana was used for this purpose. In his method, a polymerized gel as a template was used for the formation of nanoparticles. We have synthesized BAM nanoparticles with average diameter of 50 nm using polymerized gel as a template instead of cellulose. First polymerized gel was produced through the esterification process between prophylene glycol and citric acid. This gel has short length

chain compared to cellulose. Therefore, it is expected that chain length is effective on particle size.

A hydrothermal synthesis of BAM nanoparticles was performed using polymerized gel as a template. The important thing that we performed in here is the use of carboxymethyl cellulose instead of prophylene glycol. It was found that the prepared particles had a spherical shape and homogenous particle size distribution. After annealing sample at 1400 °C, the morphology of the powders retained and particles size decreased from 1 μm to ~500 nm due to densification.

In order to improve the surface states, the particles were treated with either a KOH solution and dispersion agent, individually. The KOH treated sample exhibited a 40% increase in luminescence intensity, whereas 87% increase in luminescence intensity was obtained from dispersion agent-containing sample. Although the energy transfer mechanism was not clear, the resulting increase in luminescence intensity may be originated due to passivation of surface defect with organic functional groups [2-3]. In addition, light scattering was prevented by smoothing the surface of particles with alkali (KOH) solution treatment.

References

[1] H.S. Nalwa and L.S. Rohwer, Editors, Handbook of Luminescence, Display Materials and Devices **2**, ASP Press, California, USA (2003).

[2] M. Kakihana, M. Yoshimura, Bull. Chem. Soc. Jpn., 72, 1427-1443

[3] C. R. Ronda, J. Alloys Comp., **225**, (1995) 534-537.

[4] T. Justel, H. Nikol, Adv. Mater., 12, (2000) 527-530.

[5] C. Feldmann, T. Justel, C. R. Ronda and P. J. Schmith, Adv. Funct. Mater., **13,** (2003) 511-514.

[6] C. R. Ronda, J. Alloys Comp., **225**, (1995) 534-537.

[7] C. R. Ronda, J. Lumin, 72, (1997) 49-51.

[8] K. Y. Jung and K. H. Han, Electrochem. Solid-State Lett., 8, (2005) 91-94.

[9] M. Goebbels, S. Kimura, and E. Woermann J. Solid State Chem., 136, (1998) 253-56.

[10] J. P .M. J. Verstegen, A. L. N. Stevels, J. Lumin., 9, (1974) 406-410.

[11] N. Iyi, S. Takekawa, and S. Kimura, J. Solid State Chem., 83, (1989) 8-12.

[12] J. He, T. Kunitake, A. Nakao, Chem. Mater., 2003, 15 (23), 4401–4406

[13] H. U. Anderson, M. J. Pennell and J. P. Guha, Advances in ceramics: Ceramic powder science, Am. Cer. Soc., 1987, 21.

[14] M. P. Pechini, U.S. Patent No, 3330697, July (1967).

[15] R. C. Ropp and B. J. Carroll, Inorg. Chem. 1975, 14 (9), 2199–2202

[16] G. Blasse, A. Bril, Philips Res. Repts. 2, 1966, 368

[17] H. Meyssamy, K. Riwotzki, A. Kornowski, S. Naused, M. Haase, Adv. Mater., 11(10), 840 (1999)

[18] S. Shinoyama and W.M. Yen, «Phosphors Handbook,» CRC Press, Boca Raton (1999) 192–193.

[19] C. H. Yan, L. D. Sun, C. S. Liao, Y. X. Zhang, Y. Q. Liu, S. H. Huang, S. Z. Lu, Appl. Phys. Lett., 82, 20, 3511 (2003)

[20] S. Polizzi, G. Fagherazzi, M. Battagliarin, M. Bettinelli and A. Speghini, J. Mater. Chem. 12742-747 (2002)

[21] M. Yu, J. Lin, S. B. Wang, Appl. Phys. A, 2005, 80, 353-360

[22] H. Meyssamy, K. Riwotzki, A. Kornowski, S. Naused and M. Haase, Adv. Mater., 1999, 11, 840.

[23] J. C. Boyer, F. Vetrone, J. A. Capobianco, A. Speghini and M. Bettinelli, J. Phys. Chem. B, 2004, 108 (52), 20137–2014.

[24] K. Riwotzki and M. Haase, J. Phys. Chem. B, 2001, 105 (51), 12709–12713

[25] T. Justel, H. Nikol, Adv. Mater., **12**, (2000) 527-530.

[26] C. Feldmann, T. Justel, C. R. Ronda and P. J. Schmith, Adv. Funct. Mater., **13,** (2003) 511-514.

[27] C. R. Ronda, J. Alloys Comp., **225**, (1995) 534-537.

[28] C. R. Ronda, J. Lumin, **72**, (1997) 49-51.

[29] K. Y. Jung and K. H. Han, Electrochem. Solid-State Lett., **8**, (2005) 91-94.

[30] M. Goebbels, S. Kimura, and E. Woermann, J. Solid State Chem., **136**, (1998) 253-56.

[31] J. P .M. J. Verstegen, A. L. N. Stevels, J. Lumin., **9**, (1974) 406-410.

[32] N. Iyi, S. Takekawa, and S. Kimura, J. Solid State Chem., **83**, (1989) 8-12.

[33] A. L. N. Stevels and A. D. M. Schrama-de Pauw, J. Electrochem. Soc., **123**, (1976) 691-694.

[34] A. L. N. Stevels, J. Lumin., **17**, (1978) 121-124.

[35] S. Oshio, K. Kitamura, T. Shigeta, S. Horii, T. Matsuoka, S. Tanaka and T. Kanda , J. Electrochem. Soc., **146,** (1999) 392-395.

[36] B. M. J. Smets and J.G. Verlijsdonk, Mater. Res. Bull., **21**, (1986) 1305-1308.

[37] P. Boolchand, K. C. Mishra, M. Raukas, A. Ellens and P. C. Schmidt, Phys. Rev. B, **66**, (2002) 134429.

[38] V. Pike, S. Patraw, A. L. Diaz, and B. G. DeBoer, J. Solid State Chem., **173**, (2003) 359-362.

[39] B. Dawson, M. Ferguson, G. Marking, and A. L. Diaz, J. Lumin., **106**, (2004) 39-42.

[40] T. S. Yue, A. Kai, Kenjii, K. Okazima, A. Ishizu, A. Isogai, K. Ishii, Z. Honda, Hajime, T. Shibata, T. Hirato, K. Maeda, S. Makoto and Hazime, "Functional Cellulose", (CMC Publishing co. ltd., Japan, 2003).

[41] C.W. Cho, U. Paik, D.H Park, Y.C. Kim, D.S. Zang, Appl. Phys. Lett. 2008, 93, 031505

[42] M. A. Hines, P.G. Sionnest, J. Phys. Chem., 1996, 100 (2), 468–471

[43] C. H.Yan, L. D. Sun, C. S. Liao, Y. X. Zhang, Y. Q. Liu, S. H. Huang, S. Z. Lu, Appl. Phys. Lett., 2003, 82(20), 3511.

[44] J. F. Suyver, S. F. Wuister, J. J. Kelly, and A. Meijerink, Nano Lett., 2001, 1 (8), 429–433

[45] P.Y. Lee, H. Suematsu, T. Yano and K. Yatsui, J Nanopart Res. 2006, 8,911–917

[46] S. Jenkins, S.R. Kirk, M. Persson, J. Carlen and Z. Abbas, J. Colloid Interface Sci., In Press, Corrected Proof, Available online 4 August 2009.

[47] Justin B. Hooper and Kenneth S. Schweizer, Macromolecules, 2005, 38 (21), 8858–8869.

[49] J. Park, J. Joo, S. G. Kwon, Y. Jang, T. Hyeon, Angew. Chem., Int. Ed., 2007, **46**, 4630 4660

[50] A. Dulda, M. K. Jung, W. J. Park, T. Masaki and D. H. Yoon, J. Ceram. Process Res., 2009, 10, 33-36.

[51] J. Ji, Y. Chen, R. A. Senter, and J. L. Coffer, Chem. Mater., 2001, 13 (12), 4783–4786.

[52] S Jeong, M. Achermann, J. Nanda, S.Ivanov, V. I. Klimov, and J. A. Hollingsworth J. Am. Chem. Soc., 2005, 127 (29), 10126–10127.

[53] B. C. Chakoumakos, M. Arbraham, L. A. Boatner, J. Solid State Chem., 1994, 109,197.

[54] R. C. Ropp and B. J. Carroll, Inorg. Nucl. Chem., 1977, 39, 1303−1307.

[55] H. Colfen, and S. Mann, Angew. Chem. Int. Ed. 2003, **42**, 2350 – 2365

[56] E. Rabani, D. R. Reichman, P. L. Geissler and L. E. Brus, Nature, 2003, **426**, 271−274.

[57] S. Erdei, F.W. Ainger, L.E. Cross, W.B. White, Mater. Letters, 1994, **21,** 143-147

[58] S. Zhou, G. Garnweitner, M. Niederberger, M. Antonietti, Langmuir, 2007, 23 (18), 9178–9187

[59] L. Yanhong, H. Guangyan, J. Solid State Chem., 2005, 178, 645-649.

[60] C. C. Wu, K. B. Chen, C. S. Lee, T. M. Chen, B. M. Cheng, Chem. Mater., 2007, 19, 3278-3285.

[61] M. Yu, J. Lin, S. B. Wang, Appl. Phys. A, 2005, 80, 353-360

[62] H. Meyssamy, K. Riwotzki, A. Kornowski, S. Naused and M. Haase, Adv. Mater., 1999, 11, 840.

[63] J. C. Boyer, F. Vetrone, J. A. Capobianco, A. Speghini and M. Bettinelli, J. Phys. Chem. B, 2004, 108 (52), 20137–2014.

Appendix A

Publications

1) Synthesis of rod shaped BAM nano-phosphors by a liquid phase precursor method and their luminescence properties, **A. Dulda**, M. K. Jung, W. J. Park, T. Masaki and D. H. Yoon, J. Ceram. Process Res., 2009, 10, 33-36.
2) Photoluminescence characteristics of the nano-sized red phosphor (Yx,Gdy)O3:Eu^{3+} by using liquid phase precursor methods, M.K. Jung, W.J. Park, J.W. Moon, T. Masaki, A. Dulda and D.H. Yoon, J. Korean Phys.Soc., 2008, 53, 2382-2385.
3) Morphology and photoluminescence properties of flux-grown BAM nanophosphor **A. Dulda**, D. S. Jo, T. Masaki and D. H. Yoon, J. Ceram. Process Res., 2009, 10(6), 811-816.
4) Milling effect and enhanced luminescence property of BAM nanophosphor via surface modifications **A. Dulda**, D. S. Jo, T. Masaki and D. H. Yoon, NANO, 2009, 4(6).
5) Morphology transformation and luminescence properties of $Y_{0.96}P_{0.70}V_{0.50}O_4$:$Eu_{0.1}$ nanophosphor particles **A. Dulda**, D. S. Jo, T. Masaki and D. H. Yoon, J. Ceram. Process Res.,(Submitted)
6) Surface treatment and enhanced luminescence properties of YPV:Eu nanophosphors **Ayse Dulda,** Deok Su Jo, Lyong Soon Pu, Takaki Masaki and Dae Ho Yoon (Submitted to Mater. Sci. Eng. B)
7) New synthesis technology for high efficiency $Y_{0.99}P_{0.70}V_{0.50}O_4$:$Eu^{3+}$ nanophosphor **Ayse Dulda,** Deok Su Jo, Lyong Soon Pu, Takaki Masaki and Dae Ho Yoon (Accepted J.Ceram. Soc. Japan.)

Presentations (Oral & Poster)

1) Morphology transformation of $Y_{0.96}P_{0.70}V_{0.50}O_4$:$Eu_{0.1}$ phosphor particles (Poster), **Ayse Dulda**, Deok Su Joe, Takaki Masaki, Dae Ho Yoon, "International symposium for phosphor materials, November 4-6, 2009, Niigata-Japan.

2) Synthesis of iron oxide nanoparticles with the assist of organic template (Oral), **Ayse Dulda**, Deok Su Joe, Takaki Masaki, Dae Ho Yoon, "2008 Japan-Korea workshop on nanomaterials for IT", January 15-17, 2009, Tokyo-Japan

3) Photoluminescence properties of nano-sized BaMgAl10O17:Eu phosphors by liquid phase precursor method, (Oral), **Ayse Dulda**, Mong-Kwon Jung, Woo-Jung Park, Takaki Masaki, Dae Ho Yoon, September 17, E-MRS Fall Meeting 2007, Warsaw-Poland.

4) Morphology and photoluminescence properties of flux additive $BaMgAl_{10}O_{17}:Eu^{2+}$ Phosphor by LPP Method, (Poster), **Ayse Dulda**, Mong-Kwon Jung, Woo-Jung Park, Takaki Masaki, Dae Ho Yoon, The 5th International Conference on Advanced Materials and Devices, December 12-14, ICAMD 2007, Jeju-Korea.

5) Formation of ZnO nanocrystals by vapour-liquid-solid method (Poster), **A. Dulda,** A . Erol, M.Ç. Arıkan, "23rd International Physics Congress", 13-16 September 2005, Muğla University